A Test Setup for the Investigation of Charge Transfer Processes of a GEM based TPC

Diplomarbeit

Institut für Experimentalphysik
Universität Hamburg

vorgelegt von
Bernhard Voigt

Hamburg
April 2004

Abstract

For the future e^+e^- linear collider TESLA, a Time Projection Chamber (TPC) is foreseen as a main tracking device. Instead of conventional readout, based on wire chambers, a gas amplification system using GEMs (Gas Electron Multipliers) is proposed. In this thesis a GEM based detector was employed, in order to study the charge transfer processes. A detailed description of the detector and the setup is given. The results from the measurements are compared to an existing parameterisation of the charge transfer processes. Additionally first results of the measurements of the ion feedback are discussed.

Zusammenfassung

Für den geplanten e^+e^-–Linearbeschleuniger TESLA soll als Hauptspurkammer eine Zeit-Projektions-Kammer (TPC) verwendet werden. Anstelle der konventionellen Auslese, basierend auf Drahtkammern, wird eine Auslesesystem mit GEMs ("Gas Electron Multipliers") vorgeschlagen. Im Rahmen dieser Arbeit wurde ein GEM basierter Detektor in Betrieb genommen, um Studien zum Ladungstransfer durchzuführen. Eine ausführliche Beschreibung des Detektors und des Messaufbaus wird dargelegt. Die aus den Messergebnissen berechneten Ladungstransferkoeffizienten werden mit einer existierenden Parametrisierung verglichen. Erste Ergebnisse zum Ionenrückfluss werden vorgestellt.

Contents

1 Introduction **7**
- 1.1 The Linear Collider . . . 8
- 1.2 The Linear Collider Detector . . . 10
  - 1.2.1 The TESLA TPC . . . 10
- 1.3 Aims of this Investigation . . . 12

2 Basic Principles **13**
- 2.1 Gaseous Detectors . . . 13
  - 2.1.1 Interaction of Radiation with Matter . . . 13
  - 2.1.2 Drift and Diffusion . . . 16
  - 2.1.3 Impact of a Magnetic Field . . . 19
  - 2.1.4 Gas Amplification . . . 20
- 2.2 Time Projection Chambers . . . 22
  - 2.2.1 Design and Operating Mode of a TPC . . . 22
  - 2.2.2 TPC Readout . . . 23
- 2.3 Gas Electron Multiplier . . . 28
  - 2.3.1 Geometries and Electrical Field . . . 29
  - 2.3.2 GEM Characteristics . . . 32
  - 2.3.3 Multiple GEM Structures . . . 35
  - 2.3.4 GEM and Magnetic Field . . . 36

3 Experimental Setup **37**
- 3.1 Requirements . . . 37
- 3.2 Instrumentation Overview . . . 37
- 3.3 The Detector Chamber . . . 38
  - 3.3.1 The GEM Tower . . . 41
  - 3.3.2 Employed GEMs . . . 43
- 3.4 High Voltage Supply . . . 43
- 3.5 Readout Electronics . . . 45
  - 3.5.1 Nanoamperemeter . . . 45
  - 3.5.2 Analog to Digital Converter . . . 45

3.5.3 Multiplexer 46
3.6 Control and Data Acquisition Software 48

4 Experimental Technique and Analysis 51
4.1 Performing Measurements 51
4.2 Data Analysis 52
4.2.1 Naming Conventions 52
4.2.2 Calculation of GEM coefficients 52
4.3 Systematical Errors 57

5 Results and Discussion 60
5.1 Preparative Experiments 60
5.1.1 Calibration of the USB Readout System 60
5.1.2 Steady Currents 63
5.1.3 Current Sum 63
5.2 Measurements of GEM coefficients 66
5.2.1 Electron Collection Efficiency 66
5.2.2 Electron Extraction Efficiency 67
5.2.3 Ion Collection Efficiency 69
5.2.4 Ion Extraction Efficiency 71
5.2.5 Ion Feedback 72
5.3 Russian GEMs 73

6 Summary and Outlook 75

A 77
A.1 Physical Data 77
A.1.1 Radioactive Source 77
A.1.2 Radiation Length 77
A.2 Multiplexer Circuit 78

Chapter 1

Introduction

Since the development of quantum physics at the beginning of the last century, the aim of particle physics was to describe the smallest constituents of the world surrounding us and their interactions. Up till now, the so called Standard Model (SM) gives an almost sufficient description of elementary particles and their interactions. It is based on 12 different elementary particles, classified into leptons and hadrons, their corresponding anti-particles and three interactions, the strong, the weak and the electromagnetic force. This model has been tested successfully throughout the last years in many laboratories where collisions of very high energetic particles are used to study the interactions and properties of elementary particles.

However, the SM is unsatisfactory in the sense of a simple and consistent description of particles and interactions. It contains many free parameters and has no explanation for the reason of the three different interaction forces. In addition the fourth interaction, gravitation, is neglected, although it is the dominant force in our daily life.

Therefore extensions to the SM are being discussed, e.g. Supersymmetry (SUSY), with the aim to account for these shortcomings. Physics beyond the SM is expected at energies of $\mathcal{O}(1\text{ TeV})$. Therefore a new generation of particle accelerators is needed.

The present thesis describes studies carried out for a gaseous detector which is planned to constitute the main device for the detection of charged particles at a future linear collider. After an introduction of the *Linear Collider Project* and the global framework of the thesis, in Chapter 2 the theoretical basics of gaseous detectors are described. A description of the construction of the setup used for the investigations is given in Chapter 3. In Chapter 4 the technical details of the measurements are explained, in Chapter 5 first results are discussed. Finally, a summary and outlook is given in Chapter 6.

1.1 The Linear Collider

During the last years particle physicists worldwide became more and more sensitive to phenomena occurring at energies beyond those of the available particle accelerators. Today data from accurate experiments gives a preview of exciting discoveries that may be made at higher energies. These data also allow an estimate of the parameters of a machine capable of discovering new physics. Some of the results from currently available data can only be understood by postulating new phenomena at the TeV scale. Experiments at these energies will help to explain the origin of mass and the nature of space and time.

Currently a storage ring collider, the Large Hadron Collider LHC is under construction at CERN[1]. At the LHC protons are accelerated up to a centre-of-mass energy of 14 TeV. Protons are conglomerates with a substructure of quarks and gluons and the interaction between the colliding particles is rather complicated and hence difficult to reconstruct. The energy of one proton is shared between its constituents. Therefore the initial energy for interacting components must be calculated for each event, which a priori leads to uncertainties. Thus the precision of measurements of all elementary processes and separation of all participating particles may not be sufficient to exclude or prove a theory.

Therefore a linear e^+e^- collider is planned which provides a well defined initial state and centre-of-mass energy, and thus allows a much higher precision in the reconstruction of physics events. The collider is planned to operate at a centre-of-mass energy of the order of 1 TeV.

But why a linear collider? A ring machine comes with many advantages, e.g. offering the possibility of more than one interaction region along the ring, short localised accelerating structures increasing the particle energy with each circulation and a high luminosity due to the fact that the particles are stored in ring machines.

One major problem when accelerating charged particles is the loss of energy due to synchrotron radiation when the particle transverse momentum is changed, which is the case for curved accelerators. The energy loss E_{rad} is

$$E_{Rad} \propto \frac{1}{r}\left(\frac{E}{m}\right)^4, \tag{1.1}$$

where r is the radius of the collider, E the energy and m the mass of the particle. This amount of energy has to be restored and in the case of light

[1] CERN is the European Organisation for Nuclear Research. A particle physic centre in Geneva, Swiss

particles e.g. electrons it can be very high. However, this is why the hadron collider machines are still efficient because the proton is 1800 times heavier than an electron and the energy loss is almost negligible. Another approach to obtain less energy loss is to decrease the accelerator curvature. But for desired centre-of-mass energy beyond 1 TeV the radius of the ring accelerator has to be enormous, because the energy loss is only decreased by r^{-1}. The costs to build such a ring collider are too high. This is why electron-positron colliders with a centre-of-mass energy higher than 200 GeV have to be built as linear accelerators.

There are three conceptual designs for the Linear Collider, the TESLA Project [1–4], the Next Linear Collider [5] and the Japan Linear Collider [6]. The studies presented here are carried out for TESLA, but are applicable to the other projects, too. A brief overview of the TESLA project follows.

The TESLA Linear Collider

TESLA stands for Tera Electron Volt Energy Superconducting Linear Accelerator, a project planned and designed by an international collaboration. The technical concept has already been published (TESLA Technical Design Report TDR). A sketch of the overall layout of TESLA is shown in Figure 1.1. In contrast to the other accelerator proposals, TESLA is based on a superconducting technology for the accelerator cavities. Recent tests showed field gradients for accelerating particles of 35 MeV/m, sufficient to achieve a total centre-of-mass energy of 800 GeV. One proposed location for the collider is the north-west of Hamburg. The total length of the collider is 33 km, positioned in a tunnel 10-30 m underground. The accelerated electrons and positrons are arranged in, so called *bunch trains*, consisting of 2820 single bunches, with a 337 ns time space between the bunches. The bunch trains collide at the interaction region with a repetition rate of 5 Hz. The proposed design offers the possibility of a second interaction region, where the beams collide with a crossing angle.

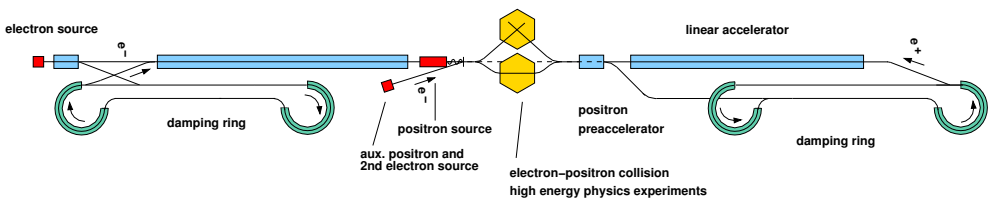

Figure 1.1: Schematic of the overall layout of the TESLA linear collider.

1.2 The Linear Collider Detector

Colliding particles with high energies produce lots of new particles. The reaction products are spread in all directions. On their flight many of them decay via cascades into further particles. From the reconstruction of the products and their properties, i.e. momentum, angular distribution, charge, energy loss and many more, one can draw conclusions about the interaction properties. From comparison with theoretical predictions, describing the interaction, a model can be either confirmed or ruled out. Determining the interaction law from such indirect evidence is not a trivial task, and therefore one must know as much as possible about the reaction products. This is the goal of particle detectors in high energy physics. Since different properties demand specialised detectors, a modern partical detector has a whole array of different devices, all read out by computers. Afterwards the data is analysed by combining the information from all detector components.

A detector for the linear collider must fulfil many requirements. The proposed detector for the TESLA project must be suitable for a broad range of particle energies from the Z–mass at 91 GeV up to 800 GeV and the detector has to deal with a high rate of reactions. The physics programme at the Linear Collider demands a good momentum resolution, a precise vertex reconstruction, a very good jet mass measurement and a excellent hermeticity [4].

Figure 1.2 shows the proposed TESLA detector. The vertex detector (VTX) close to the interaction region and the intermediate tracker (SIT) are both silicon detectors. As the main tracking device a Time Projection Chamber (TPC) is foreseen. On both ends of the TPC straw tubes serve as forward chambers (FCH). The main goal of these detectors is the precise track reconstruction and the determination of the momentum from the curvature of particle tracks in the magnetic field. Directly joining the TPC a electromagnetic (ECAL) and hadronic calorimeter (HCAL) serve for energy measurements. These inner parts are enclosed by a solenoid which produces a magnetic field of 4 Tesla (COIL). The outermost part of the detector is the muon system, which is located in the return yoke for the magnetic flux (YOKE).

1.2.1 The TESLA TPC

Time Projection Chambers are a specialised type of gaseous detectors. They have been successfully operated worldwide, e.g. in the past at LEP[2] within

[2]Large Electron Positron storage ring collider at CERN

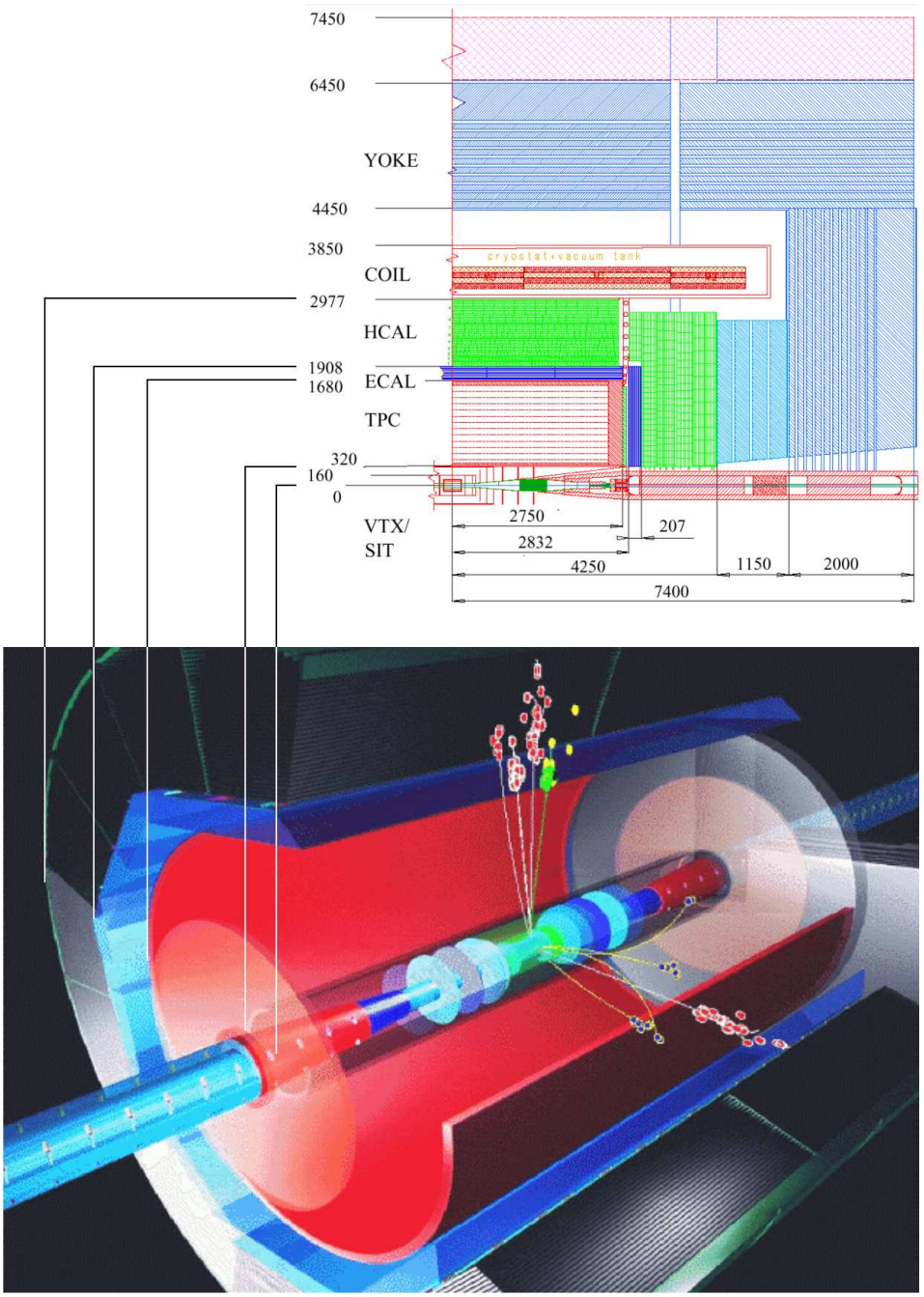

Figure 1.2: Model and schematic view of the TESLA Detector. Dimensions are in mm [1].

the ALEPH and DELPHI experiments and currently at the STAR experiment in Brookhaven National Laboratory, USA.

TPCs allow an efficient and unambiguous 3-dimensional track reconstruction with many track points and simultaneous measurement of the specific energy loss. In addition no massive material except support structures compromises the outer parts of the detector, for example the calorimeters.

According to the TDR the transverse momentum resolution will be $\delta(1/p_t) < 2 \cdot 10^{-4}(\mathrm{GeV}/c)^{-1}$. Therefore a point resolution less than 150 μm is necessary. For the energy loss a relative standard deviation of $\sigma(\frac{dE}{dx})/\frac{dE}{dx} \leq 5\%$ is specified. In order to achieve these aims the TPC is big sized, with a radius of 170 cm and length of around 450 cm. In addition the usage of new technologies for the readout system, such as Micro Pattern Gas Detectors, is favoured.

The operation principle of a TPC is introduced in Section 2.2.

1.3 Aims of this Investigation

It was intended to measure the transfer coefficients describing the Gas Electron Multiplier (GEM) characteristics and performance as introduced in Section 2.3.2. In order to carry out these measurements in high magnetic fields a new detector chamber was constructed. Hence a main goal was to verify the operativeness of this chamber. In addition a new data acquisition system with hard- and software components was built up.

In the global frame of research and development for the TESLA TPC, these investigations on GEM performances are necessary to reveal whether a GEM based gas detector is suitable for the environment present at a linear collider.

Chapter 2

Basic Principles

In order to understand the way gaseous detectors work, it is necessary to understand their basic principles. They are introduced in this chapter. After the general basics of gaseous detectors, the principle of a TPC is explained and the characteristics of GEMs are summarised.

2.1 Gaseous Detectors

Particle detectors are devices to detect sub atomic particles, i.e. elementary particles, atomic nuclei, ions and photons. This is achieved by utilising the excitation or ionisation of atoms or molecules. Gaseous detectors are one of the oldest devices, already used by Becquerel for studies of radioactive radiation. The simplest gaseous detector consist of two electrodes in a gas filled environment, with a voltage applied between them. As a result of hits with gas molecules incoming ionising particles produce free ions and electrons, which are attracted by the electrodes owing to the electrical field. The accumulated charge on the electrodes is then read out by electronic devices.

2.1.1 Interaction of Radiation with Matter

It is the particles interaction with the sensitive volume of the detector, which provides their evidence. One has to distinguish between neutral particles and charged particles, because the sensitivity of the detector is based on electromagnetic interactions. Thus neutral particles can only be detected indirectly by exploiting secondary charged particles. Photons for example are electrically neutral but they interact electromagnetically with matter and can produce secondary charged particles. Here processes other than those for charged particles are taken into account.

Charged Particles

For heavy particles ($m \gg m_e$) two processes are crucial for the energy loss when they penetrate material. These are the inelastic scattering upon molecules and atomic shell electrons and elastic scattering upon atomic nuclei. The first process accounts for the specific energy loss $\frac{dE}{dx}$, where the energy deposit leads to excited atoms or, if the energy exceeds the binding energy, to ionisation of atoms. In the second case only little energy is lost due to the large mass of the nuclei. The mean energy loss dE per length dx for heavy particles penetrating matter is described by the Bethe-Bloch formula [7]:

$$-\frac{dE}{dx} = \frac{e^2 N_A}{\epsilon_0} z^2 \frac{Z}{A} \frac{1}{\beta^2} \left[ln\left(\frac{2m_e c^2 \gamma^2 \beta^2}{I_0} \right) - \beta^2 \right] \tag{2.1}$$

e	:	elementary charge e = 1.610^{-19}C
z	:	charge of incoming particle in units of e
Z, A	:	atomic number and weight of absorbing material
m_e	:	electron mass
ϵ_0	:	dielectric constant
N_A	:	Avogardo's Number
I_0	:	effective ionisation potential
β	:	β-factor of incoming particle
γ	:	$\gamma = \sqrt{1-\beta^2}$

The energy loss shows (see Fig. 2.1) a characteristic decrease, which falls as $1/\beta^2$ and reaches a minimum around $\beta\gamma = 3$. Due to relativistic effects it continues with a logarithmic rise, until reaching the *Fermi plateau*. According to the relation $\beta = \frac{p}{mc}$ simultaneous measurements of specific energy loss $\frac{dE}{dx}$ and momentum p allows a particle identification. Since Formula 2.1 is independent of the particle mass, the energy loss separates for different particle masses as a function of the particles momenta.

The figure shows a different energy loss for electrons. Here the energy loss is mainly governed by Bremsstrahlung for high energetic electrons. Bremsstrahlung is induced by deflection of electrons in the electrical field of the nuclei. Whilst for low energies the energy loss is also governed by scattering, the behaviour of electrons is identical to heavy particles. More details can be found in [8].

Photons

There are three different interactions of photons with matter, depending on the photon energy E_γ:

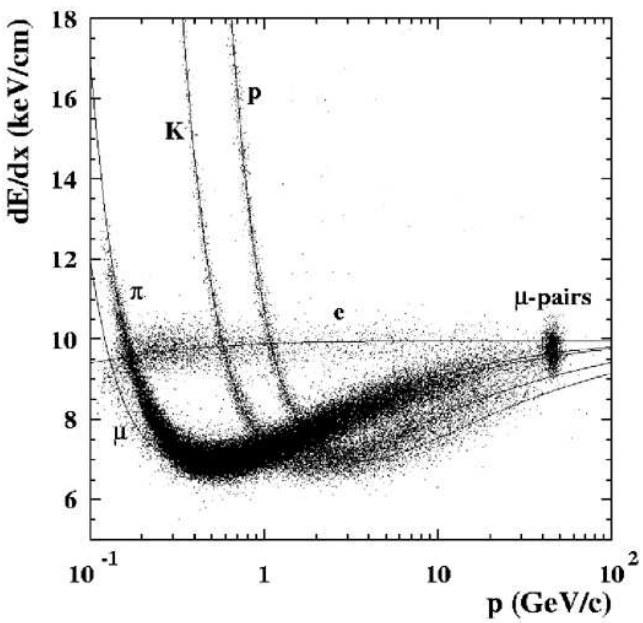

Figure 2.1: Measurement of energy loss for several particles as function of momentum at OPAL. This plot is based on [9].

- **Photoelectric effect** ($E_\gamma \leq 0.5$ MeV) describes the ionisation of atoms, when an incoming photon energy exceeds the binding energy for shell electrons, whereby the total photon energy is deposited.
- **Compton scattering** ($E_\gamma \sim 1$ MeV) is the absorption of a fraction of the photon energy, when scattering at atomic electrons. In comparison to the photon energy the binding energy of the electron is negligible, hence the scattered electron can be treated as free and the energy transfer depends on the scattering angle.
- **Pair production** ($E_\gamma > 1.1$ MeV) occurs when the photon energy exceeds the energy to produce an electron–positron pair. However, this cannot take place in vacuum owing to momentum and energy conservation.

The cross sections for these processes strongly depend on the photon energy. Figure 2.2 shows the total cross section per atom, as well as the cross sections for individual processes.

Due to the interactions, the intensity I_0 of an incoming photon beam is reduced. As a function of length x the intensity I decreases exponentially:

$$I(x) = I_0 e^{-\mu x}, \tag{2.2}$$

where μ is the mass absorption coefficient given by

$$\mu = \frac{\sigma N_A}{A}, \tag{2.3}$$

with N_A being Avogardo's Number, A the molar mass and σ the photon cross section. The absorption length is defined as the length after which the initial intensity is decreased to I_0/e.

2.1.2 Drift and Diffusion

In gases the motion of free charge carriers like electrons and ions is governed by diffusion and drift. The drift arises from an external electrical field and diffusion from thermal zitterbewegung and scattering with gas molecules. Electrons and ions differ in their movement because of their different masses.

Drift

Under the influence of an electrical field positive ions and negative electrons drift in opposite directions, which leads to their spatial separation. The drift

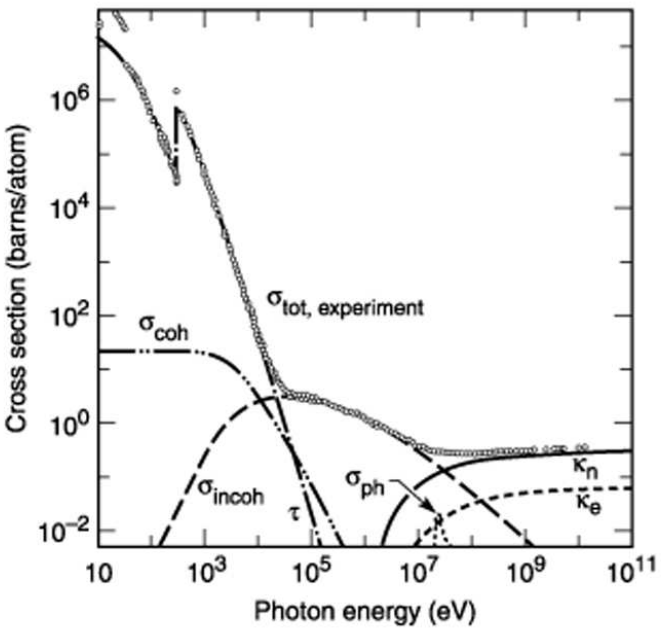

Figure 2.2: Total photon cross section σ_{tot} in carbon, as a function of energy, showing the contributions of different processes. The processes, which were described in the text are: τ atomic photo-effect (electron ejection, photon absorption), with the typical spring, when the energy level of a atomic shell is reached; σ_{incoh} incoherent scattering (Compton scattering off an electron); κ_n pair production (nuclear field). Here, the other cross sections are not significant. Details can be found in [10].

velocity for ions is hardly influenced by collisions, due to their large mass. It depends on field strength E, mobility μ^+ and pressure p (normalised to normal pressure p_0):

$$v^+_{Drift} = \mu^+ E \frac{p_0}{p} \tag{2.4}$$

In contrast, subjected to collisions with gas molecules, electrons partially loose their accumulated kinetic energy. The mobility depends on the electrical field and the mean free path length ($\propto 1/\tau$). Thus the drift velocity reaches an equilibrium very fast. According to Townsend the drift velocity for electrons is given by [11]

$$v^-_{Drift} = \frac{e}{2m_e}\tau E \ . \tag{2.5}$$

Diffusion

Diffusion occurs as a result of the thermal energy of electrons. Therefore the electron energy ϵ is given by the Maxwell-Boltzmann-distribution:

$$F(\epsilon) = const \cdot \sqrt{\epsilon} e^{-\frac{\epsilon}{kT}} \tag{2.6}$$

ϵ	:	mean thermal energy, being $\epsilon = 3/2kT \approx 0.04$ eV under normal conditions
k	:	Boltzmann's constant
T	:	temperature

Assuming the simplest case of an isotropic distribution, electrons from a point-like cloud, after having drifted some time, will have a Gaussian density distribution:

$$\frac{dN}{dx} = \frac{N_0}{\sqrt{4\pi Dt}} e^{-\frac{x^2}{4Dt}} \tag{2.7}$$

N_0	:	total number of charges
x	:	distance from origin
D	:	gas specific diffusion coefficient

Hence the diffusion width is given by

$$\sigma = \sqrt{2Dt}. \tag{2.8}$$

The diffusion constant D depends on gas properties as well as the drift velocity and the masses of the diffusing particles. Hence it is obvious that

electrons and ions have different diffusion characteristics, where the width of the ion distribution is smaller than that of electrons. For drifting charges in electric fields the assumption of an isotropic diffusion is no longer true. The diffusion constant is split into a transversal and longitudinal part, D_T and D_L respectively. They depend on the electrical field strength [11].

2.1.3 Impact of a Magnetic Field

Under the influence of a magnetic field both the drift and diffusion of moving charged particles is governed by the Lorentz-Force

$$\vec{F} = q\vec{v} \times \vec{B} \ . \tag{2.9}$$

For parallel electric and magnetic fields only the transverse diffusion of particles is affected, since the vector product vanishes for $\vec{v}_{drift} \parallel \vec{B}$. The magnetic field forces the charge carriers to follow the arc of a circle. This decreases the transverse diffusion by

$$D_T(B) = \frac{D_0}{1 + \omega^2\tau^2} \ . \tag{2.10}$$

Here D_0 is the diffusion coefficient in the absence of a magnetic field, ω denotes the cyclotron frequency with $\vec{\omega} = e\vec{B}/m$ and τ is the mean time between collisions of the drifting particle with a gas molecule.

However, near to amplification structures magnetic field components exist perpendicular to the electrical field. Thus the drift velocity is no longer parallel to the electrical field. The angle between the velocity $\vec{v}_{drift}$ and the electrical field $\vec{E}$ is defined as the Lorentz-Angle α_L and given by

$$\tan(\alpha_L) = v_{drift}\frac{B_\perp}{E} \ . \tag{2.11}$$

Under the influence of a magnetic field the drift velocity is described by the Langevin formula [11]:

$$\vec{v}_{drift} \propto \hat{\vec{E}} + \omega\tau\left(\hat{\vec{E}} \times \hat{\vec{B}}\right) + \omega^2\tau^2\left(\hat{\vec{E}} \cdot \hat{\vec{B}}\right)\hat{\vec{B}}, \tag{2.12}$$

where $\hat{\vec{E}}$ and $\hat{\vec{B}}$ are unit vectors of the fields.

The second term increases with magnetic field strength and owing to the vector product, it changes the particle drift direction.This leads to a lack of precision in determining the position of the primary ionisation. This effect is often called $\vec{E} \times \vec{B}$ effect. Owing to the large mass of ions, the deflection is small in comparison to electrons and hence the second term has no such impact. The last term gives a contribution along the magnetic field lines. As it increases with B^2 it is dominant for high magnetic fields.

2.1.4 Gas Amplification

For gaseous detectors the amount of charge produced by ionisation is not sufficient to obtain a signal, which can be read out electronically. If the electrical field the electrons are subjected to is high enough, gas amplification can be utilised to produce a higher signal: an electron is accelerated in an electrical field, if it gains an energy higher than the ionisation potential of the gas molecules, it produces electron-ion pairs along its path. In turn these secondary electrons are also accelerated and acquire enough energy to ionise the gas and again for the next generation of electrons and so on. This results in an avalanche process, described by an exponential function:

$$N(x) = N_0 e^{\alpha x}, \tag{2.13}$$

where N_0 is the number of primary electrons, x is the distance from their origin and α the Townsend coefficient, which gives the probability of ionisation per unit path length. The Townsend coefficient is related to the mean free path λ according to $\alpha = 1/\lambda$ and depends on the gas properties such as temperature and pressure, as well as on the electrical field strength.

The gain is given by the ratio between the total number of electrons after amplification and the number of primary electrons. From Eq. 2.13 follows the gain for a distance $\overline{AB}$ as

$$G = \frac{N(x)}{N_0} = \exp\left(\int_A^B \alpha(x)dx\right). \tag{2.14}$$

Figure 2.3 illustrates the gain dependency as a function of the applied potential. As labelled in the graph, different operational modes are possible. At a low potential recombination dominates, but at a slightly higher field, the free primary electrons are affected and attracted to the anode. Simple *ionisation chambers* work in this region. By further increasing the applied potential, the *proportional region* is reached. Under the circumstances of negligible space charge, caused by slower travelling ions, the energy loss of primary ionising particles is proportional to the collected charge after amplification. A gaseous detector like a TPC is operated in this region. In the *limited proportional region*, the accumulated space charge is no longer negligible and causes local changes to electrical field such that, the strict proportionality is lost. Further increase of the electric field finally leads to electrical breakdown of the gas. Space charges shield the external field, so no charge separation occurs and recombination takes place, yielding secondary photon emission and many secondary ionisation avalanches. If this process propagates, a chamber is said to work in the *Geiger-Müller mode*. *Continuous discharge* happens when the field strength is high enough to affect the

entire gas. The ionised gas molecules and free space charges realize electrical conduction between the anode and cathode.

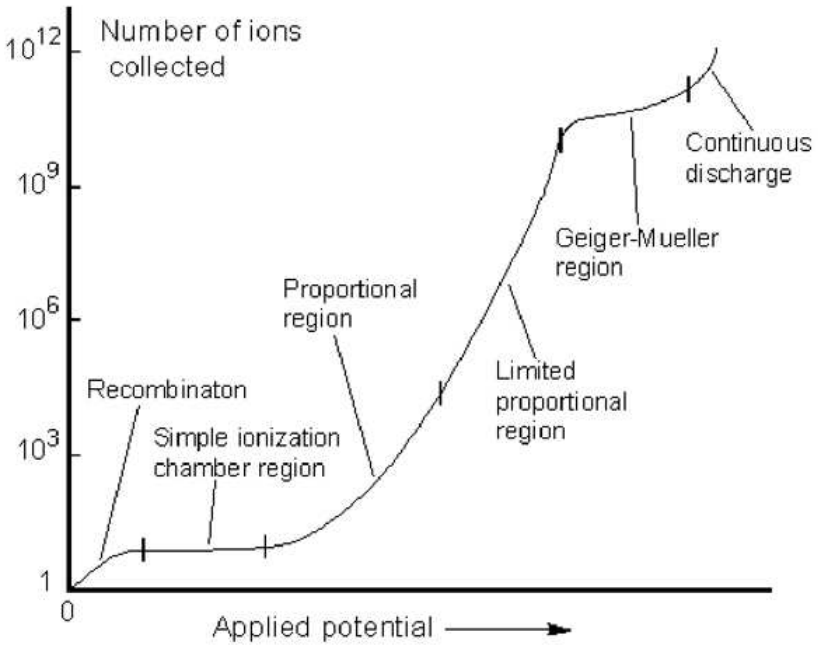

Figure 2.3: Gas amplification as a function of the applied potential. The different regions of operation are shown [12].

Typically gas amplification sets in at field strength of a few 10kV/cm. In proportional mode gains of up to 10^6 are possible.

Detector Gas

In principle all gases can be used for generating electron avalanches, if the applied electrical field is high enough. However, depending on the intended use of the detector, specific requirements such as gain or good drift and diffusion characteristics limit the choice of gases or mixtures.

Noble gases for example offer sufficient amplification at comparatively low fields, in contrast to complex molecules. Adding other components always increase the threshold voltage before amplification happens. However, noble gases do not permit operation at sufficiently high gains without electrical breakdown. When the atoms excited within the avalanche process return to their ground state, photons are emitted at energies high enough to initiate further avalanches. This problem is solved by adding a *quenching gas* which

absorbs energetic photons. Often organic gases are used, having a high cross section for photo-absorption over a broad wavelength band. The molecules dissipate the excess energy either by elastic collisions, vibration and rotation or by dissociation into simpler radicals. Whereby the latter process is not desired, because of aging effects of the detector components.

In addition impurities from outgassing structural materials or from the outside atmosphere, diffusing through leaks, change the operational properties. For example a minor contamination of oxygen in the range of parts per million (ppm) leads to considerable loss of electrons by gathering them, because of the electron negativity of oxygen.

2.2 Time Projection Chambers

Time Projection Chambers, first proposed by Nygren [13], belong to the type of drift chambers. Using drift chambers, allows to reconstruct three dimensional particle tracks and determine the specific energy loss dE/dx, exploiting that a charged particle will leave a 'track' as it ionises atoms along its path. In addition, in the presence of a magnetic field, it is possible to measure the momentum of the particles perpendicular to the magnetic field. The track of charged particle is curved owing to the impact of the magnetic field and the track curvature is proportional to the momentum of the particle. In the following some more details on design, operation principles and readout technologies of TPCs are given.

2.2.1 Design and Operating Mode of a TPC

A time projection chamber (see Fig. 2.4) consists of a gas filled chamber, terminated with a high voltage cathode plane and low potential or grounded anode plane. The electrical field between these electrodes is called the *drift field*, where electrons and ions produced by ionisation travel towards the corresponding electrode. The surrounding walls are covered with electrodes with a potential gradient applied, such that they form a field cage to produce a homogeneous electrical field over the entire volume.

To reconstruct a track of an ionising particle, which passes the gas filled volume, the projection of charges on the endplate is used. In particular the electrons are used, which drift to the endplate under the influence of the electrical field. This provides information about the x-y coordinates. The z-coordinate along the drift field is obtained by measuring the time the electrons need to travel from their origin to the endplate. Since the drift velocity is constant in a homogeneous field, the time between transit of the

ionising particle t_0 and arrival of electrons at the readout plane t_{Signal} gives the distance between the particle track points and the endplate.

$$z = v_{Drift}\,(t_{Signal} - t_0) \tag{2.15}$$

This principle of track reconstruction is illustrated in Fig. 2.4.

In case of colliding beam experiments, the high voltage cathode is often located in the symmetry plane of the detector at the interaction point, orthogonal to the beam axis. Two readout endplates close the chamber on both sides (Fig. 2.5). A magnetic field parallel to the beam axis for the determination of particle momentum is provided by a solenoidal magnet.

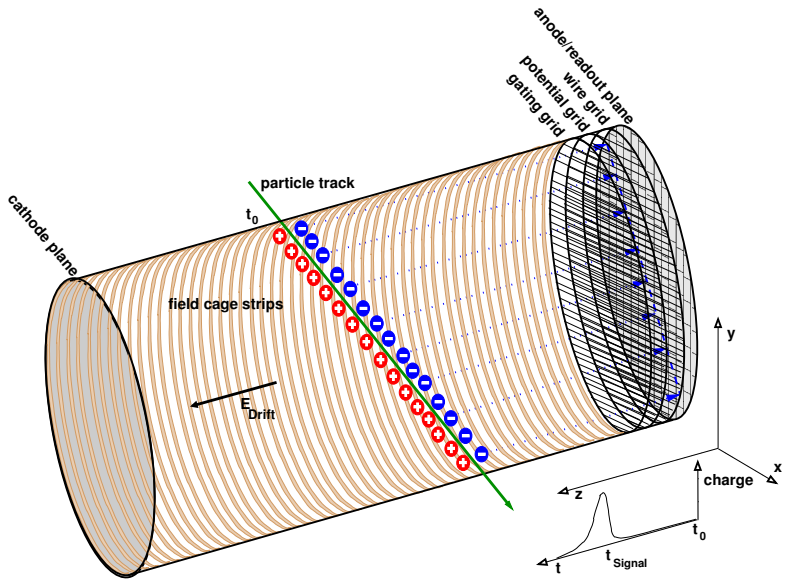

Figure 2.4: Illustration of the measurement principle of a TPC.

2.2.2 TPC Readout

In order to reconstruct the x-y coordinates the anode plane is segmented into pads, typically with an area of the order of mm^2. Each pad has its own readout electronic chain consisting of preamplifiers, shapers and digitisers. From the pad location and the signal distribution over the affected pads, coordinates in x-y plane are calculated. The time measurement is started either from external triggers, or, if operated in beam colliding experiments, from the time of the particle collision. A counter takes the time until a signal is detected by the readout electronics. From the x-y coordinates and the time

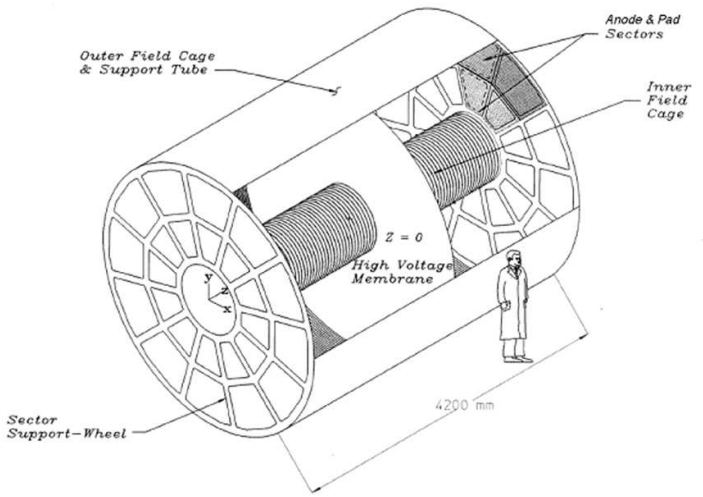

Figure 2.5: Schematic view of the STAR TPC [14].

information a computer calculates charge clusters. From a track fit to these clusters the traversing particle path is determined.

For the gas amplification, necessary for the readout, conventionally thin wires have be used successfully for gas amplification. In the recent past new developments have been made, so-called *Micro Pattern Gas Detectors* (MPGD), to improve the operation capabilities of TPCs. In the following both techniques are described.

Multiwire Proportional Counters (MWPC)

The readout structure in MWPC is composed of three layers of wires (see Fig. 2.6). Starting from the anode, the first layer of wires is the sense wire grid used for gas amplification and readout. The wires are operated in the proportional mode. The induced positive signal on the segmented readout plane is recorded, in order to reconstruct the x-y coordinate of the ionisation (Fig. 2.7). The signal is spread over multiple pads and for the track reconstruction a Gaussian fit is applied to the charge distribution. The resulting coordinates for the centre of charge have an accuracy limited by the width of the distribution. In addition the negative signal on the wires can be read out.

The potential grid shields the electrical field in the drift volume from the high field of the sense grid and ensures a stable and homogeneous drift field. The uniformity of the drift field is of prime importance for an accurate

track reconstruction. Indeed, the distortions from ions, which remain in the sensitive volume in a huge amount due to the gas amplification, are not negligible. Although a large fraction is neutralised on the sense and potential wires, the amount of positive charge left in the drift volume destroys the field uniformity. This *ion feedback* is reduced almost to zero by the gating grid. For "gate open" state the grid is at a potential given by its location, in order to not disturb the drift field. For the "gate close" state a potential difference between the wires is applied in a way that a dipole field is created, which stops the ions from travelling into the drift volume.

This concept requires a triggering of the gating grid between the particle bunch collisions. For TESLA, however, a continous mode operation of the TPC is required, because the time between particle bunches is too short.

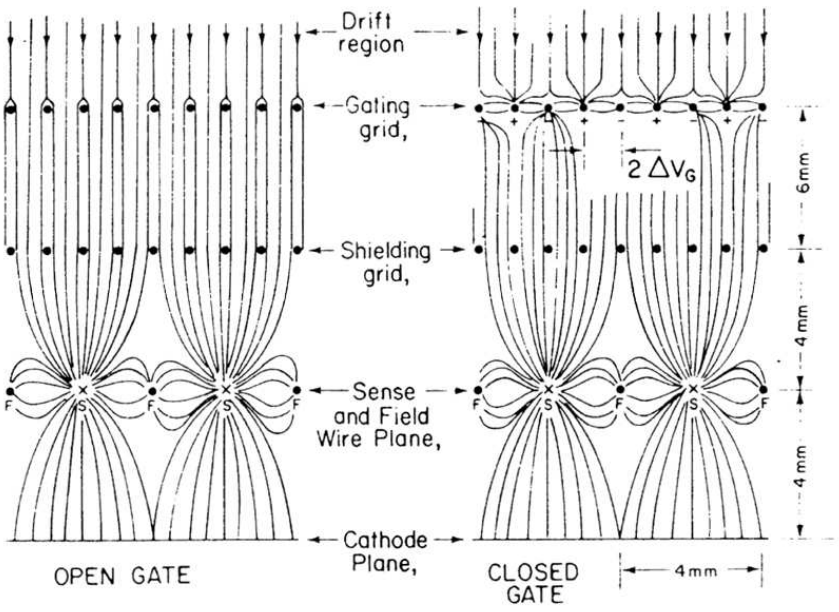

Figure 2.6: Electric field lines with gate in "open state" and in "close state" [15].

In addition $\vec{E} \times \vec{B}$ effects caused by the non linear field line alignment close to the wires reduce the resolution. In order to avoid sagging of the wires, they are mounted under tension. Thus the support structures for the end cap of the TPC has to be constructed of strong and solid material.

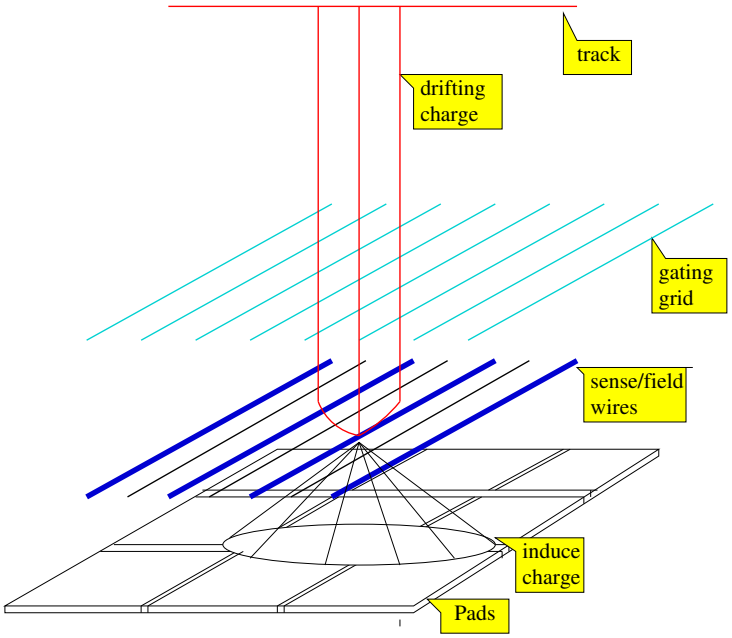

Figure 2.7: Wire readout in MWPC [4].

Gas Electron Multiplier Readout

An attractive alternative to wire based readout components is based on MPGDs, such as *Gas Electron Multipliers* [16]. Here the usage of GEMs in gaseous detectors is introduced. In the following Chapter 2.3 the properties and characteristics of GEMs are discussed.

GEMs, first introduced in 1997 by F. Sauli and the Gas Detector Development Group (GDD [17]) at CERN, consist of a thin metal clad polyimide foil, with a high density of chemically pierced holes $\mathcal{O}(\mu\text{m})$. To use a GEM as an amplifier a potential difference of a few hundred volts must be applied between the conducting copper films, resulting in a field strength of several 10 kV/cm in the holes. This is sufficient to obtain gas amplification inside the holes.

As in a MWPC gaseous detector the drift field forces the electrons to the readout plane, where the electrical field in near the GEM surface accelerates the electrons into the holes (see Fig. 2.8). Usually a stack of two or more GEMs is used to increase the total gain and improve the operational stability. When using highly different electric fields in front and behind the GEM, an intrinsic suppression of ion feedback can be exploited. After the last GEM, like in MWPC, a segmented anode plane picks up the signal.

In contrast to MWPC the signal on the readout plane is the electron charge cloud itself and not the signal produced by the positive ions. Hence it is more accurate, improves the time resolution as well as the determination of primary ionisation position. But, as the total number of readout channels is limited the pad size is large and only single pads collect the charge. Hence the point resolution is limited by the pad size, in contrast to MWPC where the point resolution is given by the width of the charge distribution. Developments, investigating sophisticated pad geometries [18] or placing resistive foils on the top of the pads to obtain charge sharing due to additional spread of the charge cloud are ongoing.

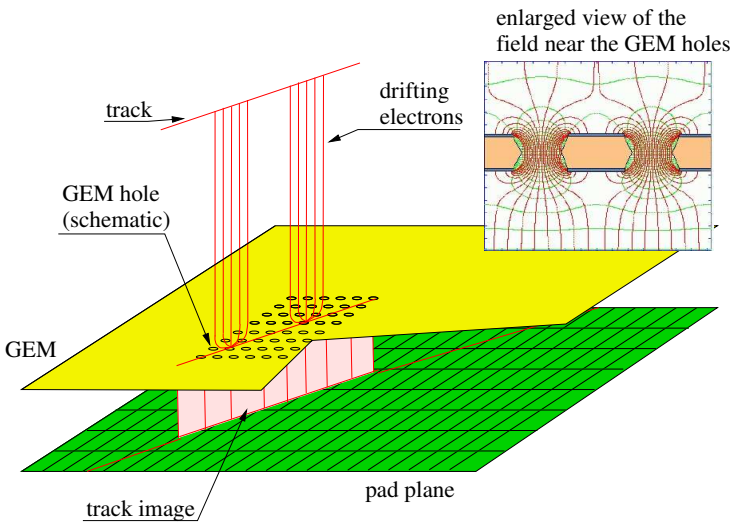

Figure 2.8: Schematic view of GEM readout system [4]. In the upper right picture the electrical fields near the GEM holes is shown [19].

Apart from the high intrinsic resolution capability, GEMs offer several further advantages compared to wire readout systems. Because of the small structures, the regions where $E \times B$ effects arise, are in the order of μm, thus the point resolution is increased. As GEMs have a symmetric two dimensional geometry in the x-y plane, they do not have a preferred direction, the resolution over the complete readout area is uniform. One major benefit is the intrinsic suppression of ion feedback, which makes this detector particularly suitable for a high rate event environment. Finally, no mechanically heavy support structure is needed for the assembly of GEMs.

Alternative Readout Technologies

Micro Mesh Gaseous Structures, Micromegas [20] offer an alternative MPGD device, schematically shown in Fig. 2.9. A uniform high electric field is produced between a thin metallic mesh stretched at a distance of 100 μm above the readout pad plane. With a very high electric field ($\sim$ 30 kV/cm) across the gap, electrons arriving form the drift volume of the chamber are collected and multiplied in the gap and read out at the pad plane. Like GEMs, Micromegas have also no preferred direction and an intrinsic reduction of ion feedback, as well as no significant $E \times B$ effects.

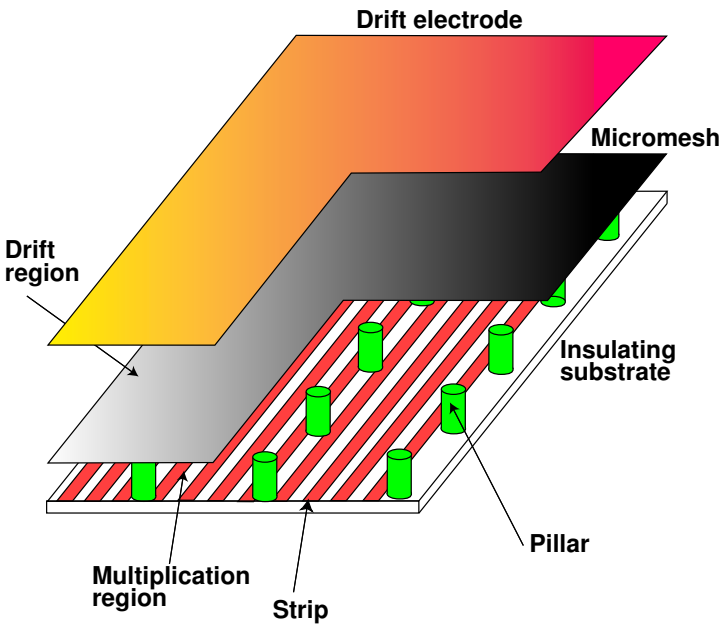

Figure 2.9: Schematic layout of a Micromegas. [4].

2.3 Gas Electron Multiplier

As mentioned above a GEM is a composite of a supporting insulation polyimide foil and two copper layers on each side pierced with holes. Commonly Kapton®[1] is used, having a small electrical conductivity of $0.6{\cdot}10^{-17}\Omega^{-1}\mathrm{cm}^{-1}$, an electrical permittivity between three and four and a magnetic permeability around one. Standard GEMs are produced in a double mask process [16].

[1] Kapton® is a registered trademark of E. I. du Pont de Nemours and Company

The pattern of holes is first engraved by conventional photolitography on the metal on both sides of the foil. In following steps the channels through the foil are etched, using a Kapton® specific solvent, whereby the copper openings are used as a mask. Due to the chemical process employed, dissolving the unprotected polymer from both sides, the holes have a double-conical shape with the diameter in the centre of the insulator slightly smaller than that at the metal surface. A electron microscope photograph of a GEM hole cross section is shown in Fig. 2.10.

However, depending on the production methods, among the double-conical shabe, other geometries are possible. These are conical shapes, where the diameter constantly decreases over the thickness of the GEM, and a cylindrical shape, where no change in diameter over the cross section is desired. Typical values for the thickness of the Kapton®foil and the copper are 50 μm and 5 μm, respectively. Hole diameters vary over a range between 40 μm to 140 μm with distances between them from 90 μm to 200 μm.

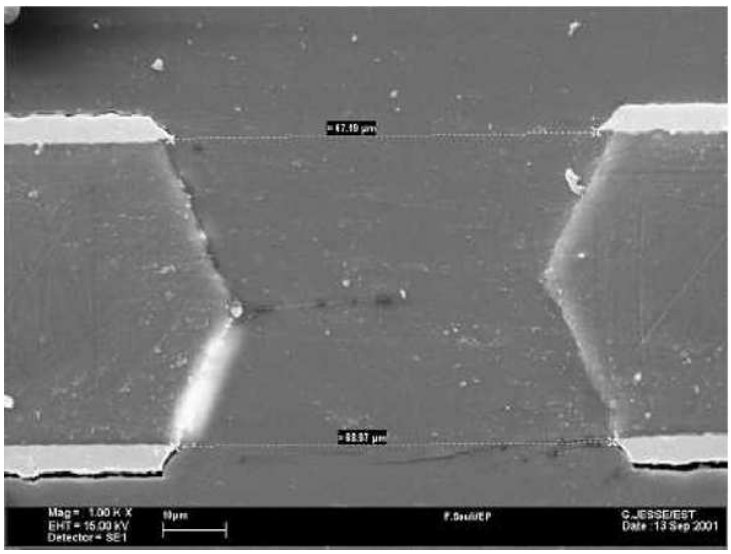

Figure 2.10: Cross section through a hole. The double-conical shape is characteristic of the chemical etching of the polymer [17].

2.3.1 Geometries and Electrical Field

The relevant geometrical parameters of the so-called *Standard-GEM* are shown in Fig. 2.11. A hexagonal alignment of holes is shown with a double conical hole shape, having a copper diameter D of 70 μm and in the

middle of the Kapton®foil a diameter d of 65 μm. The distance between the holes (pitch) P is 140 μm. The optical transparency T_{opt} of the GEM mesh, i.e. the ratio of open to total area, is given by

$$T_{opt} = \frac{\pi}{2\sqrt{3}} \left(\frac{D}{P}\right)^2 . \tag{2.16}$$

For the standard GEM T_{opt} is around 0.23, but may be less, since the inner

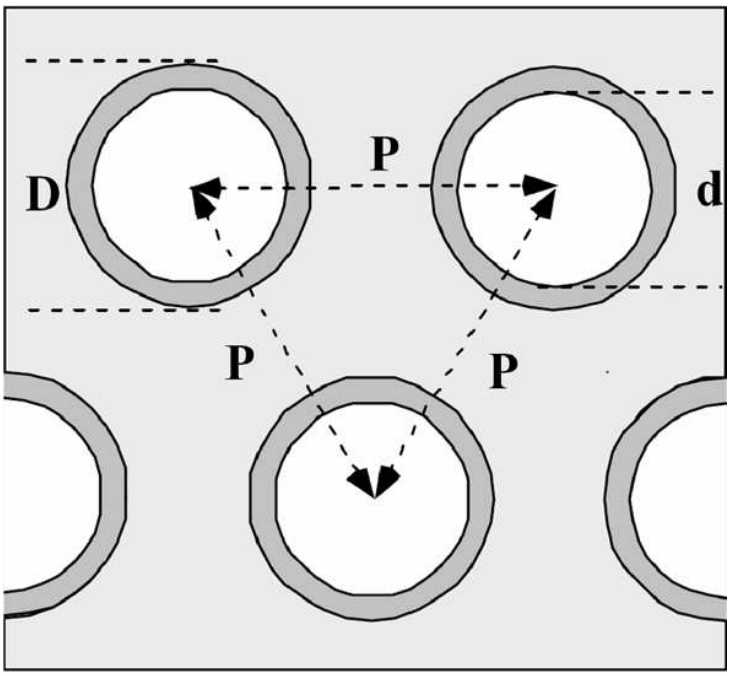

Figure 2.11: Schematics of the standard GEM geometry [21].

hole diameter is smaller. For electrons, passing the GEM, the important quantity is the electrical transparency. This depends on the applied fields, as they influence whether the electrons are pulled through the holes or not.

An important parameter of a GEM is the mean electrical field inside the hole E_{hole}. It is defined as the integral of the electrical field over the area of the hole centre A [22]:

$$E_{hole} = \frac{\int_A \vec{E} d\vec{a}}{\int_A d\vec{a}} \tag{2.17}$$

Considering that a GEM is a capacitor an estimation of the field strength inside the holes can be made. A homogeneous dipole field in the polyimide is

created depending on the applied voltage U across the copper surfaces, there the field strength is given by

$$E = \frac{U}{d}. \tag{2.18}$$

The electrical field inside the hole is approximately the same as in the polyimide, because of electrostatic connection conditions, where $E_{\parallel}$ is continuous from a dielectric into the vacuum.

The field gradients inside the GEM hole are plotted in Fig. 2.12 and Fig. 2.13. It is obvious that the high fields along the copper edges may cause sparks due to spontaneous field emissions, if the GEM voltage is too high [21].

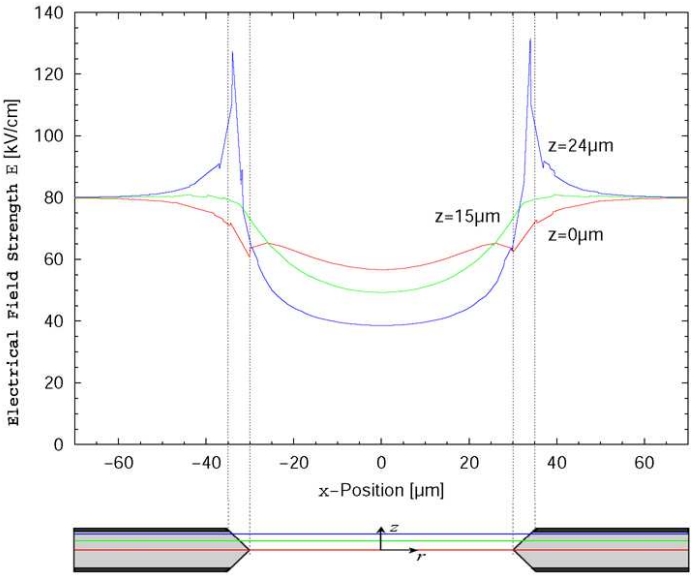

Figure 2.12: Shape of electrical field strength along the central x-axis through a GEM hole for different levels [23].

Simulations [23] and measurements [24] of the electrical field inside the GEM holes show a dependence of the GEM geometry, the voltage across the GEM foil U_{GEM}, the electrical fields of the drift region E_D above and the induction region E_I below the GEM. A parameterisation is given by a linear ansatz, where a and b are free parameters, determined by the GEM geometry:

$$E_{hole} = a\, U_{GEM} + b\,(E_D + E_I) \tag{2.19}$$

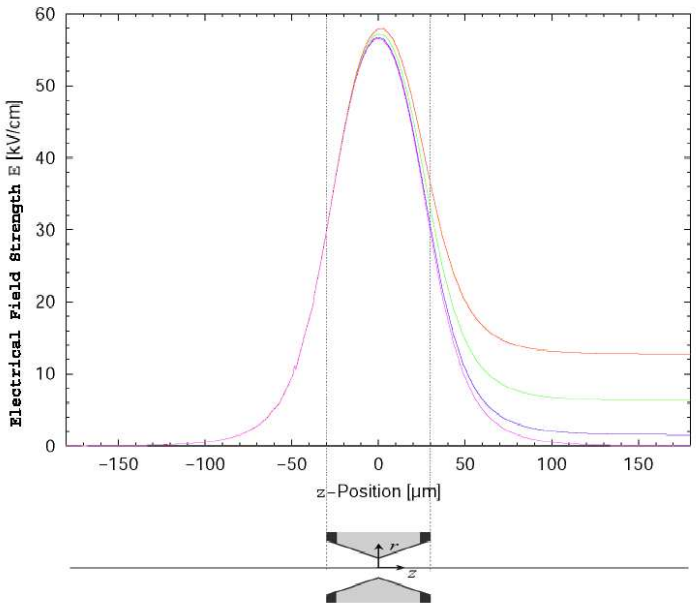

Figure 2.13: Shape of electrical field strength along the central z-axis through a GEM hole for different external fields [23].

2.3.2 GEM Characteristics

As discussed above in the parameterisation of the electrical field inside the GEM holes (Eq. 2.19), in a detector electrical fields are present above and below the GEM. These fields and the voltages across the GEM determine the properties of the detector. In Fig. 2.14 it is shown, that depending on the external field strength not all field lines are collected inside the GEM holes. For the high field below the GEM a part of the electrical field lines end up on the copper surface of the GEM. In contrast, for the low field above the GEM, all field lines are collected inside the GEM holes. Hence, it is possible that not all charge carriers produced in the drift region enter the GEM hole and not all charge carriers produced in the GEM holes reach the induction region. To study these charge transfer properties the so-called *transfer coefficients* are introduced [22].

Transfer Coefficients

Transfer coefficients describe the behaviour of charge carriers, i.e. electrons and ions, when they pass a GEM hole:

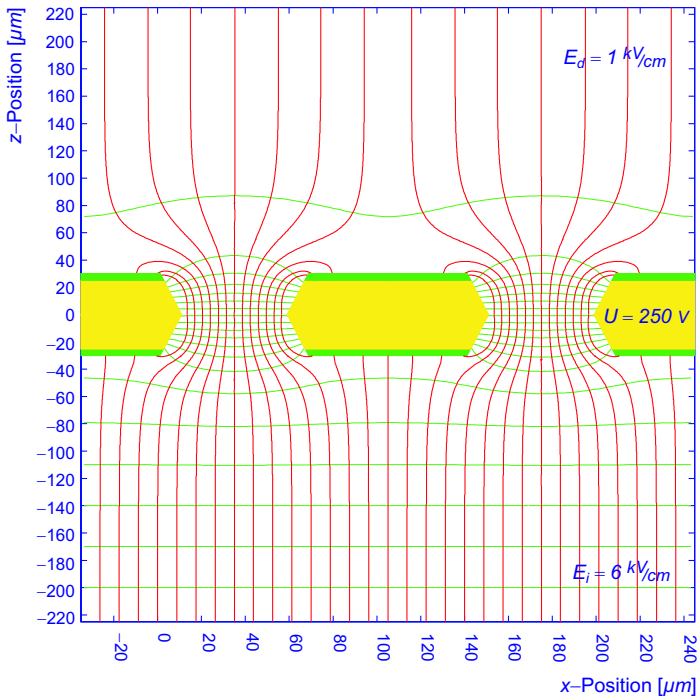

Figure 2.14: Shape of electrical field lines in a GEM with external fields of 1 kV/cm above and 6 kV/cm below [23].

- The *collection efficiency* $C^{-(+)}$, i.e. the fraction of electrons (ions) collected into the GEM holes per number of electrons (ions) arriving.

- The *gain*, G, i.e. the factor by which the number of electrons is increased by gas multiplication inside the GEM holes.

- The *extraction efficiency* $X^{-(+)}$, i.e. the fraction of electrons (ions) extracted from the GEM holes into the chamber volume per number of electrons (ions) produced in the holes.

- The *secondary extraction efficiency* X^{+}_{sec}, i.e. the fraction of ions extracted from the GEM holes into the chamber volume per number of ions which had been collected inside the holes. This differs from the primary extraction X^{+}, it describes the *electrical transparency*.

- The *effective gain* G_{eff} is defined as $C \cdot G \cdot X$, given that only a combination of coefficients is accessible by measurements. And the gain itself cannot be determined.

Ion Feedback

The ion feedback is rather a property of the detector than a GEM characteristics.

- The *ion feedback* IF is the fraction of ions reaching the cathode per number of ions produced in the amplification process.

Considering that the drifting charges cannot be measured directly, the coefficients and the ion feedback have to be calculated from corresponding currents on the electrodes (see Section 4.2).

Parameterisation

The coefficients can also be expressed as ratios of electrical fluxes. From simulations a parameterisation for the collection efficiency is obtained, as well as for the extraction efficiency [23]:

$$C = \begin{cases} 1 & \text{for} \quad E_{ext}/E_{hole} \leq r^{1/s} \\ r\,(E_{ext}/E_{hole})^{-s} & \text{for} \quad E_{ext}/E_{hole} > r^{1/s} \end{cases}, \tag{2.20}$$

$$X = \begin{cases} \frac{1}{T_{opt}}\,(E_{ext}/E_{hole}) & \text{for} \quad E_{ext}/E_{hole} \leq r^{1/s} \\ \frac{r}{T_{opt}}\,(E_{ext}/E_{hole})^{1-s} & \text{for} \quad E_{ext}/E_{hole} > r^{1/s} \end{cases}, \tag{2.21}$$

where E_{hole} is the electrical field inside the GEM holes, E_{ext} the field below or above the GEM and T_{opt} the optical transparency of the GEM.

Following equation 2.22 describing the gas amplification, a parameterisation is given by a simple exponential ansatz with the free parameters α and β:

$$G = \beta e^{\alpha E_{hole}} \tag{2.22}$$

Table 2.1 summarises the computed parameters for a standard GEM.

Parameter	Error
a=156.414 cm^{-1}	$\pm 0.005\ cm^{-1}$
b=0.0590	$\pm 4 \cdot 10^{-6}$
r=0.1831	± 0.0028
s=0.5174	± 0.0059
α=$1.64 \cdot 10^{-4}$	$\pm 1.64 \cdot 10^{-5}$
β=$9.6 \cdot 10^{-3}$	$\pm 9.6 \cdot 10^{-4}$

Table 2.1: GEM parameters computed from simulation [23].

2.3.3 Multiple GEM Structures

In the simplest case a GEM based detector consists of a cathode, a GEM foil and a segmented anode plane. The applied voltages determine the operation properties of the GEM, i.e. extraction and collection efficiencies for electrons and ions, as well as the gain of the gas amplification.

A gas amplification of around 10^4, is required for an effective detector operation which in turn demand a high GEM voltage. The operational safety and lifetime stability of a GEM decreases with increasing applied voltages, because the sparking probability increases. Thus it is practical to use two or more GEMs in a cascade, yielding high gains with lower voltages across the individual GEMs, with the effect of decreasing the rate of electrical breakdowns over the GEMs. To a good approximation the properties of several GEMs in cascade can be derived from the properties of a single GEM system [21].

It is assumed that the alignment of GEM foils with respect to the hole pattern is not relevant, as the diffusion of electron clouds between two GEMs is in the order of millimetres [25]. Hence, the electron cloud leaving a GEM hole is spread over several holes of the next GEM and the number of collected electrons is determined by the collection efficiency of the second GEM.

2.3.4 GEM and Magnetic Field

As already mentioned in Section 2.1.3, for a GEM the $\vec{E} \times \vec{B}$ effect is very small and has only marginal effect on the resolution.

However, the operational properties in a high magnetic field environment have to be studied. It can be seen from last term in the Langevin formula (Eq. 2.12) that the electron drift velocity has a contribution along the magnetic field lines. As this term is proportional to B^2 the drift direction of the electrons in high magnetic fields is no longer given by the electrical field, but the magnetic field lines. As a result most electrons could not be collected inside the GEM holes, yet follow the magnetic field lines perpendicular to the GEM surface and eventually end up on the GEMs copper coating. Those charges will be lost for the signal and consequently decrease the dE/dx capabilities of the chamber, due to the loss in primary ionisation statistics [22].

Chapter 3

Experimental Setup

In the following, the requirements upon the experimental equipment is summarised. Then follows a detailed description of the detector and its internal setup, and finally, the deployed electronic and software components are described.

3.1 Requirements

Since the currents from primary ionisation are very small, and the ion feedback current should be of the same order, the instrumentation for the measurements of the charge transfer coefficients and subsequently for the measurement of the ion feedback must be able to measure such currents with good accuracy. This is accomplished using nanoamperemeters. In order to optimise the configuration of a GEM readout, a flexible assembly of GEMs is necessary and adjustable settings of electrical fields in a wide range are essential. This requires an internal detector setup, where the distances between the GEMs and the electrodes can be varied easily. In addition an individual high voltage supply for each electrode facilitates the settings of the electrical fields to arbitrary values.

3.2 Instrumentation Overview

A sketch of the test environment with its components is shown in Fig. 3.1. The detector houses the GEMs and electrodes. The electrical fields and GEM voltages are adjusted by a high voltage supply (HV-Supply). Each electrode is protected by a 10 MΩ resistor, limiting the current when electrical shortcuts occur. A radioactive ^{55}Fe source emitting photons with an energy of 5.89 keV ionises the gas between the anode and the first GEM. The resulting

currents are measured individually from each electrode by a CUMO (Current Monitor). The output signals from the CUMOs are switched by a multiplexer (MUX) to an analog to digital converter (ADC). A computer controls the multiplexer and reads the digitised data, as well as setting the HV-Supply.

The readout system used in this setup was made available by RWTH[1] Aachen. A detailed description of this equipment can be found in the diploma thesis of S. Lotze [26]. Later the ADC and the multiplexer were replaced by new devices and the data acquisition software was reimplemented (see Section 3.5 and 3.6).

3.3 The Detector Chamber

The detector used in this setup is an upgrade of a previously operated Mini-TPC used for current measurements [27]. In order to continue the investigations in a magnetic field, it was replaced because the old detector chamber did not fit into the magnet opening.

The mechanical structure of the detector chamber is shown in Fig. 3.2. It is constructed of aluminium and stands at 22 cm long with a diameter of 25 cm. The lids on both ends of the cylinder are gas tight sealed with O-rings. Twelve high voltage connectors serve as electrical connection of the GEM tower inside the chamber. The radioactive source can be positioned over a Kapton®window on one side of the cylinder, allowing most of the photons to penetrate the chamber volume. A carriage is mounted on the side of the chamber, which is controlled by a pneumatic pump. When the source is placed on the carriage, this allows the operator to control the exposure of the chamber to the radioactive source.

Gas terminals on each lid enable a continuous gas flow through the chamber. For this purpose a gas tank is connected via a pipeline to the 'gas in' terminal. After flushing the chamber, the gas is vented through the 'gas out' terminal, which is followed by a long pipeline, into the environment. Depending on the setup it was possible to control the gas pressure within the chamber[2].

A photograph of the opened chamber is shown in Fig. 3.3. The GEM tower is attached to the lid of the chamber. It is mounted on four nylon bars such that the radiation sensitive volume is positioned on the level of the window. The electrodes are connected to the external electrical high voltage connectors using insulated wires.

[1] Rheinisch-Westfälische Technische Hochschule

[2] This was done using an electronically adjustable vent (Bronkhurst Hi Tech SN M2207)

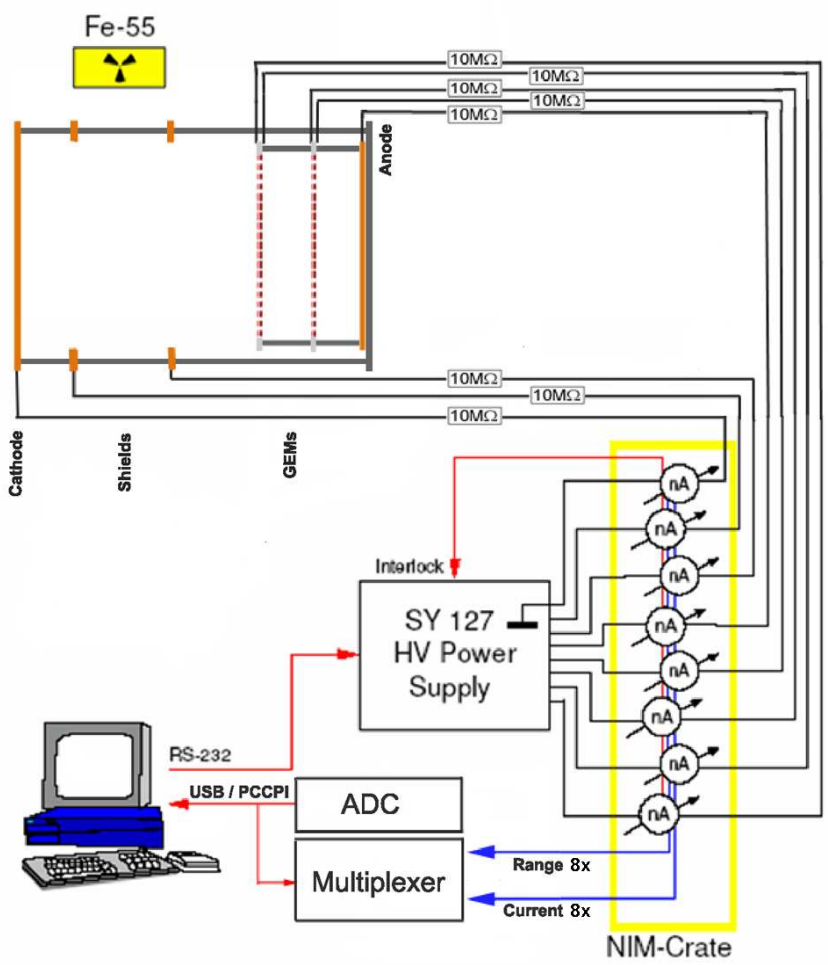

Figure 3.1: Sketch of the experimental setup.

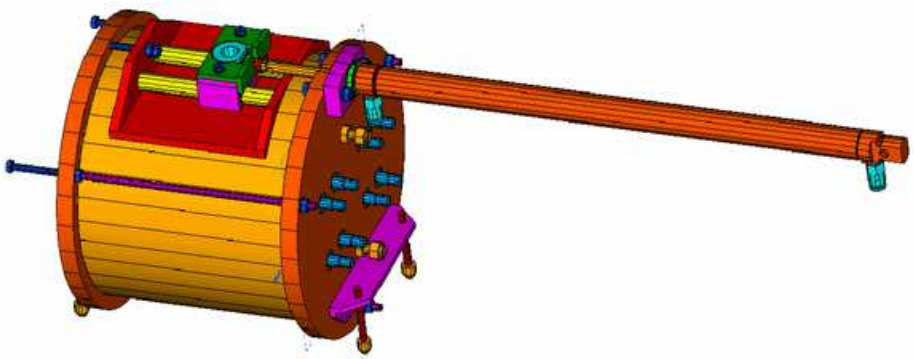

Figure 3.2: Engineering drawing of the detector. The detector chamber was built by K. Gadow.

Figure 3.3: Photography of the opened chamber with the GEM tower mounted on the lid. On the front of the vessel the carriage and the Kapton® window are visible.

3.3.1 The GEM Tower

Figure 3.4 shows a schematic view of the GEM tower. It consists of a cathode, two field cage rings, two GEMs and an anode. The rings surround the drift region and build a basic field cage. This ensures a homogeneous drift field, which is essential, because of lateral incoming radiation. Due to the fact that most of the ionisation occurs on the outer edge of the GEM tower an inhomogeneous drift field could cause loss of charge.

The distances between the electrodes can be varied. In the basic setup, the distances are 2 mm between the anode and the second GEM, as well as for the distance between the GEMs. The drift region has a height of 19.5 mm and the sensitive area of the GEMs is approximately 100×100 mm.

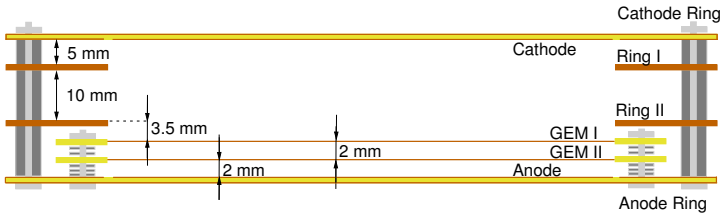

Figure 3.4: Schematic sketch of the GEM tower.

The first GEM tower design employed only one ring. It was found that the field was not homogeneous enough (see Section 5.1.3). Results from simulation of the GEM tower field configuration showed that a GEM tower with two rings would significantly increase the uniformity of the electrical field in the drift region, in particular at the edges (Fig. 3.5). Details on the simulation follow below.

The GEM tower is put together using nylon screws and nuts. Spacers and washers allow an accurate $\mathcal{O}(0.5\text{ mm})$ determination of the distances between the electrodes. Four threaded bars in the corner of the base anode board support the rings and the cathode. The GEM frames are mounted separately on four inner screws. The equality of level is an important issue, thus, to prevent sagging in the middle, a tension of the GEM foils in the frames is necessary.

For the measurements of the charge transfer only the charges in the volume inside the field cage are relevant. Here, in principle, as the field is homogeneous and no charges are lost, all charges produced can be collected. Since the cathode also covers the rings, it has to be segmented into two parts. Then the area above the drift region can be read out individually. The area above the rings is called the cathode ring. In addition, to prevent charging

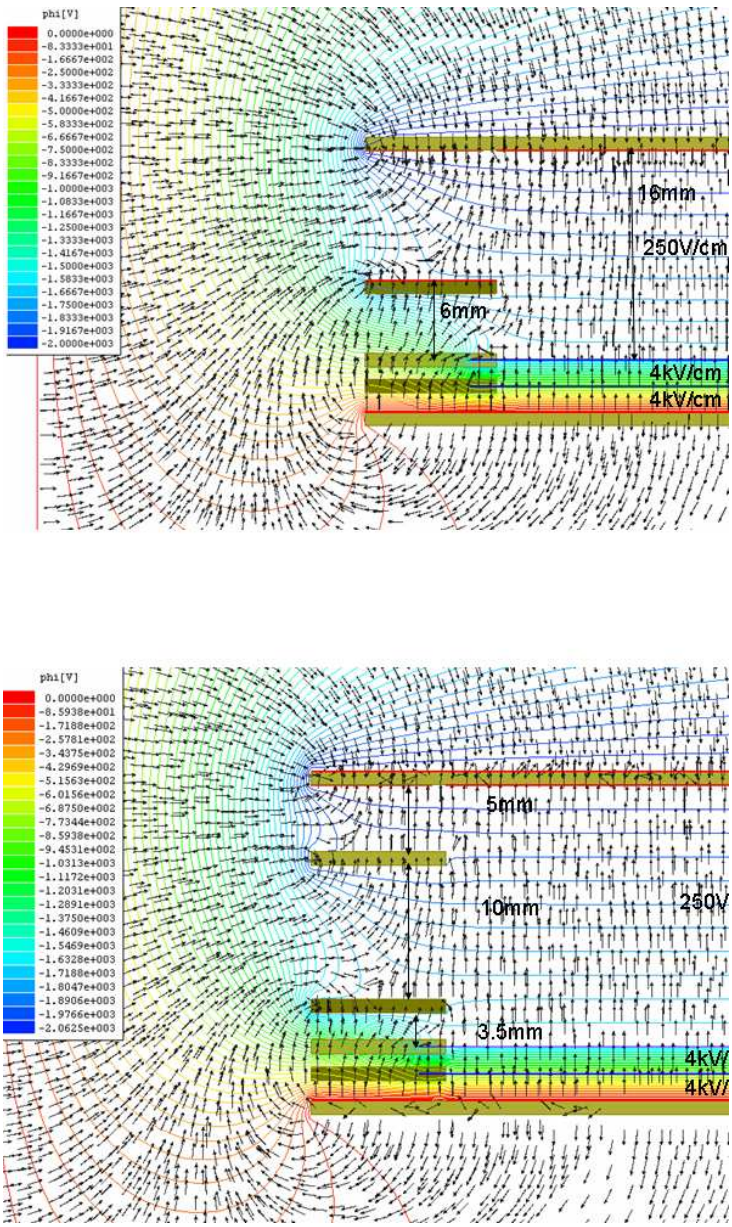

Figure 3.5: Electrical field configuration for the GEM tower. In the upper picture the first version with one ring is shown. Minor distortions below the ring on the edge of the drift region between the cathode and the first GEM are visible. In comparison, for a GEM tower with a second ring positioned lower, the homogeneity is improved.

up effects, the area on the top of the cathode is connected to the ring. The anode is constructed in a similar fashion.

Simulations for the GEM tower

The simulations have been done using Maxwell® [28], a software for the simulation of electromagnetic fields. The first step was the design of a simple model of the GEM tower. Therefore a graphical user interface allows the drawing of components and selection of materials of the GEM tower. After defining the potentials on the surfaces, a finite element solver calculates the electrical field strengths. Various properties of the final solution can be plotted. The main interest for the GEM tower is the field alignment, which is displayed as non scaled vector arrows (Fig. 3.5). In addition potential lines with a colour coding are plotted. In the figures only the outer fragment of the GEM tower is shown, since the inner field region is absolutely homogeneous. In contrast to the two ring version, the one ring GEM tower has apparent field uniformities in the region below the ring.

3.3.2 Employed GEMs

For the measurements of two different GEM types are employed. These are Standard-GEMs manufactured by the Gas Detector Development Group at CERN and GEMs produced in Nijniy Novgorod (Russia). The Russian GEMs have comparable geometry parameters to the CERN GEMs, though with a different inner hole diameter of 30 μm.

3.4 High Voltage Supply

The detector has an individual high voltage connection for each electrode. The field configuration is such that the anode is grounded. The applied negative potentials increase from bottom to top.

The high voltage supply is provided by a high voltage module manufactured by CAEN[3], type A432, installed in the high voltage system SY127 [29]. This high voltage module allows negative voltages of up to 6 kV with maximum currents of 200 μA. To avoid damage due to failures, the maximal current can be limited: if, due to a spark through a GEM hole, the current maximum is exceeded, the high voltage channel is switched of immediately (the channel trips). In order to inhibit enormous potential differences between the tripped channel and the still enabled channels, a trip signal can be

[3]Costruzioni Apparecchiature Elettroniche Nucleari, http://www.caen.it

forwarded to all channels. In such case the high voltage system automatically shuts down all channels.

Especially for testing purposes, the detector was operated using a potential divider, because of security reasons. In this case only one high voltage channel operates the whole chamber and the voltages cannot be varied individually. However, this means, if one electrode exceeds a current limit and the channel is shut down, all electrodes are grounded implicitly. In Fig. 3.6 the circuit diagram of the potential divider is shown.

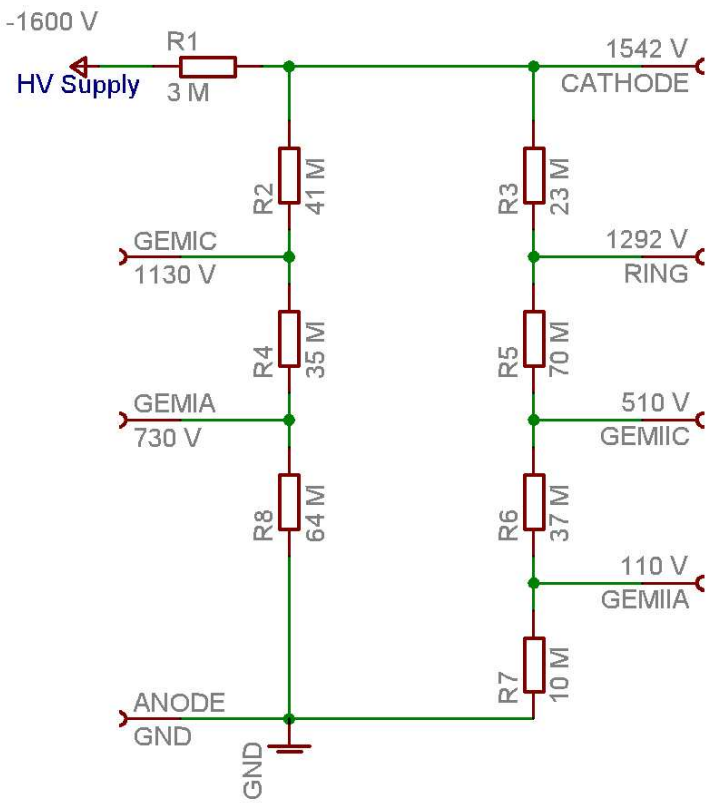

Figure 3.6: Schematic circuit diagram of the potential divider. The potential divider was used for the first GEM tower with only one field cage ring. The voltages for the different electrodes are adjusted to a typical field configuration of 250 V/cm drift field, 1 kV/cm transfer field and 1 kV/cm induction field. The voltage across each GEM is set to 400 V.

3.5 Readout Electronics

In principle for the readout only amperemeters with a visual display are necessary. But for convenient usage, a computer driven data acquisition is preferred. Therefore an ADC is used to convert the analog output signal from the amperemeters to digital data, which can be read by a computer. As the number of input channels of the ADC is limited, it is reasonable to use a multiplexer. By switching one selected analog channel to the ADC input, the multiplexer facilitates the usage of only one ADC channel for multiple analog signals.

3.5.1 Nanoamperemeter

The amperemeters (CUMO V3.0) deployed in the setup were manufactured by the III. Physics Institute of the RWTH Aachen [30]. They are built as NIM[4] modules. The current measurement precision is limited to 0.01 nA. The modules can be operated up to 7 kV. The current range can be set manually or automatically. For electronic aided data acquisition two output connectors are available. The actual current is delivered as a DC Signal between -2 V and +2 V. In order to convert this voltage to a current value, the information about the selected range must be acquired from the other output. The range is delivered as a voltage starting with 2 V for the smallest range and decreasing in steps of around 0.5 V.

3.5.2 Analog to Digital Converter

Two different ADCs have been employed during the measurements. The ADC manufactured by Dornier-System, type Do 200-1106 is implemented as a CAMAC[5] module. The input range is ±5 V and the resolution 12 Bit [31].

As another ADC a LabJack®measurement box was employed. It is a modern USB[6] device, combining several functionalities, e.g. analog and digital Input/Output and a counter. It has an input range of ±10 V and a resolution of 12 Bit [32]. The main advantage of this device is the USB interface, giving the opportunity to use this device with any modern desktop PC. A

[4]Nuclear Instrument Module, a standardisation for electronic devices

[5]Computer Aided Measurement and Control, an interface defining a data bus technology for control and data transfer from electronic devices to computers. In this setup a combination of a DBCC Crate Controller, manufactured by the III. Physical Institute of RWTH Aachen, and a PCCPI card for the PC-ISA slot was used for the communication with the CAMAC devices. Details can be found in [26].

[6]Universal Serial Bus

set of appropriated software drivers is necessary for the communication (see Section 3.6).

3.5.3 Multiplexer

In combination with the CAMAC ADC a multiplexer was used, which was also implemented as a CAMAC module. To abandon the CAMAC devices, and the PC card at the bottom of system, it was replaced when the USB ADC was introduced. Therefore a in house made device was developed with the help of an electronic engineer, Mr. Koch. The basic idea was to utilise multiplexer IC chips, which can be operated without any other electronic components. With its overvoltage protection (up to 70 V peak to peak) and the CMOS address logic, the Burr-Brown MPC506A 16 to 1 analog multiplexer, is well suited for this application, where the analog signal originates from external equipment [33]. Two of theses ICs were used to implement a 32 to 1 multiplexer.

The electronic circuit diagram is shown in Fig. 3.7. In addition to the multiplexer ICs an operational amplifier OP27 is used as a buffer on the output line (OUT). Without amplification this amplifier only acts as an impedance converter, avoiding high load on the multiplexer. The output of this IC is protected against overvoltages using the diodes connected to the power supply. The channel selection for switching the multiplexer is done by applying a binary coded number to the address input connectors (ADR). All ADR lines are connected to both multiplexer address input pins, although the most significant Bit (Bit 5) selects the multiplexer IC via the 'enable' pins. The hex inverter IC guarantees that only one multiplexer is enabled. Hence, a binary coded number between 0 and 31 selects the correlated input channel (IN). In order to avoid floating of the input lines, they are all grounded across resistor networks. The device resides in a NIM module, providing power supply connections ($\pm$12 V) and a well defined ground potential.

The multiplexer is controlled using the digital output ports from the LabJack®measurement box. They deliver CMOS specific potential levels and are directly connected to the address input lines of the multiplexer.

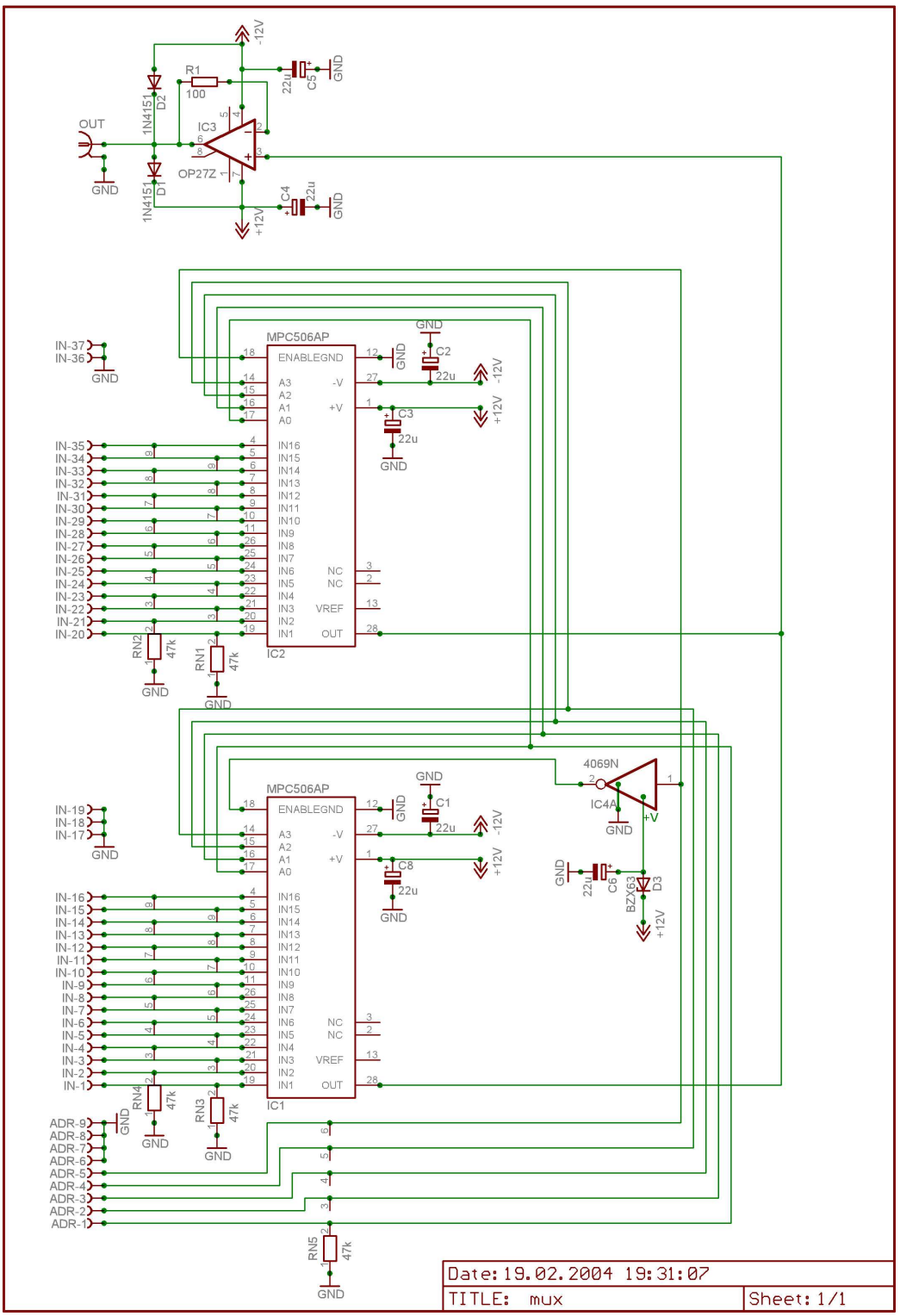

Figure 3.7: Schematic circuit diagram of the multiplexer. The diagram was designed using the electronic layout software Eagle®.

3.6 Control and Data Acquisition Software

Together with the technical equipment from RWTH Aachen software (xtc) for the data acquisition was supplied. This software was developed in C++ by S. Lotze and M. Killenberg. It provides a graphical user interface (GUI) based on the X-Window system under Linux to control and monitor the hardware components.

The control of the high voltage system SY127 was realised using an RS-232 interface. This terminal connection allows a computer aided setting and monitoring of the high voltage channels. Different text based control statements are sent via the serial port to the SY127. From the reply, a textual screen, information about the channel states can be obtained. For this the xtc software utilised a C++ class, developed by A. Nowack [34].

The communication with the CAMAC crate controller for the multiplexer and the ADC is based on an available CAMAC driver for Linux [35].

Since the program was developed for a test chamber without field cage rings, difficulties were encountered when setting the ring voltages to arbitrary values. With small modifications to the xtc sources, the detector could be operated.

The Java Test Chamber Environment (JTC)

As the ADC and the multiplexer were replaced by the new devices, major changes to the software were required. Additionally extra features that were not available in the existing software were desired. Therefore the decision was made to develop a new software suite. The USB interface of the ADC is commonly supported by any modern desktop PC, thus the software should not limit this advantage. Hence the Java [36] programming language was used for the development. In Java implemented drivers for both, the LabJack®with USB interface [37] and RS-232 serial port [38] are available.

Virtual Device Layer and Hardware Driver

In addition to the drivers for the communication with LabJack®and SY127 HV-Supply, high level drivers were implemented to map the basic functionalities of the hardware devices to software functions. For example the CUMO driver implements a method for reading the actual current. This method uses the LabJack®driver framework to access the I/O ports to switch the multiplexer and to read the current and range voltages from the output connectors of the Cumo and combines this values to deliver a current in ampere units.

However, the application only uses virtual devices for monitoring, setting and data processing. Virtual devices provide an interface, which is independent of the hardware. They only utilise the methods provided by the high level driver. Hence, when the hardware components are exchanged, the application does not have to be changed, as long as a new high level driver maps the new hardware environment to the requirements of the virtual device.

Model-View-Control Pattern

The software is designed using the *Model-View-Control Pattern*. A separation of GUI components and the underlying data structures, as well as a splitting of the controlling functionality. The model in this architecture serves as a container and obtainer for data. For example this may be a virtual CUMO device. The graphical user interface is notified when the model changes, and then interrogates the model for the new data to be displayed. The controlling part, which reacts on user interactions, is commonly implied in the GUI component. However, as the control is done by an automatic task, it is separated. This facilitates a GUI design without knowledge of the data processing, as well as data processing without the knowledge of visualisation. The software structure is easy to understand is easily extendable. Another advantage is to extend easily the number of views. A model can have multiple views, for example a GUI and a file. Neither the GUI has to know anything about the file, nor the file about the GUI. The model simply notifies all views from its list of views, which react according to their structure.

The Java API provides a basic scheme to implement the model-view paradigm. This is done by implementing subclasses of the `Observable` class (model) and implementing the `Observer` interface for the view.

Threads

Another issue is the responsiveness of the GUI. If not explicitly treated, the GUI is 'frozen' during the hardware interrogation. For example, when integrating over many measured values, this can take a few seconds,. To avoid this, threads can be used. A thread is in principle an autonomous process, which is scheduled by the operation system. If the hardware interrogation is performed by an independent thread, the processor time is shared between this and the GUI thread[7]. Thus, the GUI remains responsive. In addition if each task gets its own thread, the current high voltage state can be obtained, while the currents are read from the ADC, or the data is written to a file.

[7]Of course there are many other threads from other running processes, scheduled by the operating system, all sharing the processor time.

Everything seems to be in parallel, as the scheduler changes the threads fast enough. Again the Java API provides a framework for the usage of threads. In this software, it is used to start new threads, when the time consuming hardware interrogation is performed.

Chapter 4

Experimental Technique and Analysis

In the following a short overview of the performance of measurements is given. A section about the analysis describes how the GEM parameters are obtained from the current measurements. Finally the systematic errors are discussed.

4.1 Performing Measurements

Before the measurements are carried out, the chamber is connected to the gas system and flushed for a time of approximately 3 hours. This guarantees a pure atmosphere inside the chamber. If the equipment was available, the gas pressure is adjusted approximately 10 mbar higher than atmospheric pressure, to guarantee a determined pressure and a continuous gas flow, even if the environment pressure increases slightly. A regulation of the gas temperature is not applied. Two different gases were used four the measurements. These are a mixture with 93% argon (Ar), 5% methane (CH_4) and 2% carbon dioxide (CO_2) as proposed in the TDR, designated as TDR gas, and a Ar-CH_4 (95:5) gas.

The electrical fields and voltages are applied using the software tools. Before the radiation source is positioned over the window of the chamber, the 'blind currents' from the electrodes are recorded. This leakage currents, caused by contaminations on the electrical connectors or currents across the GEM holes or the surface of the GEM tower, are in the order of 1 nA. They are subtracted from the currents measured when the radioactive source ionises the gas.

The recording of currents is started by the software. The actual voltages and currents are written to text files. The data is plotted using gnuplot [39].

4.2 Data Analysis

In Section 2.3.2 the transfer coefficients were introduced as ratios of the transfered amount of charge carriers. In the analysis the currents are taken into account, which obviously correspond to the amount of charges.

Using the coefficients, all currents on the GEMs, cathode and anode can be expressed as a function of primary ionisation. Inversely, with these expressions the coefficients can be derived from the currents on the corresponding electrodes. However, the equations are rather complicated if more than on GEM is concerned. It is easier to extract the equations for the coefficients directly by considering the relation between the currents. Before this is carried out, the naming scheme is introduced.

4.2.1 Naming Conventions

In Figure 4.1 the names of the currents, fields and voltages are described. The GEMs are labelled from top to bottom starting from GEM1. Accordingly the GEM voltages are called $U_{GEM1,2}$ and the fields $E_{Hole1,2}$. The drift field E_D resides between cathode and GEM1. The field between the GEMs is called the transfer field E_T. The induction field E_I is the electrical field between the last GEM and the anode.

The currents on the electrodes are related to the electrodes, i.e. I_C for the cathode, I_A for the anode. As each GEM has two electrodes, they are distinguished by their orientation to the cathode and anode, respectively. Thus the currents on the electrodes directed to the cathode are designated $I_{GEM1,2_C}$ and the currents on the opposite side $I_{GEM1,2_A}$.

Sometimes it is necessary to distinguish the currents of electrons from the ion currents. In this case the currents are denoted as I^- and I^+ for the electron and ion currents, respectively.

The sign of the currents is defined by the direction of the technical electric current. Electron currents from the high voltage supply to an electrode, are regarded as positive. This means that incoming ion currents from the chamber are measured as positive currents and electron currents on the electrodes as negative currents.

4.2.2 Calculation of GEM coefficients

First some technical details are explained, in order to understand the equations for the calculations of the GEM coefficients.

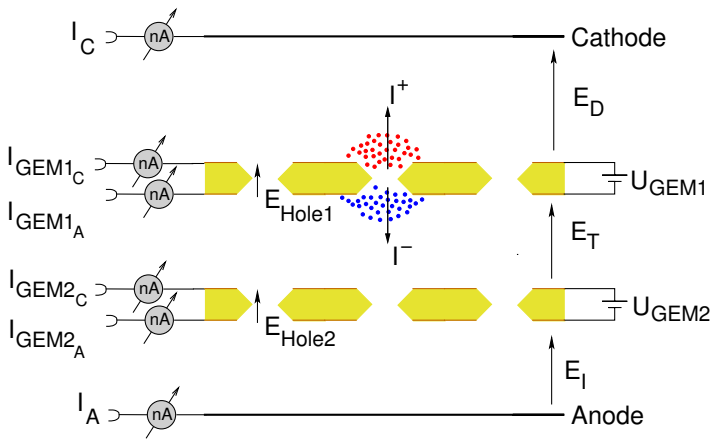

Figure 4.1: Schematic illustration of a double GEM structure with cathode and anode. The names used in the calculations are specified.

GEM Hole Electric Field Correction

The parameterisation for the electrical field within the GEM holes (Eq. 2.19) takes into account that the electrical fields on either side of the GEM contribute to the electrical field in the hole. The amplification G depends on the field strength inside the GEM hole (see Eq. 2.22) and therefore the change of an external field influences the amplification, G'. Thus, the direct determination of the GEM coefficient is misleading, because the current measurements are affected by the change of the field strengths. Therefore, the current has to be normalised by a correction factor Γ, which reflects the implicit change of the amplification [26]:

$$\Gamma\left(\Delta E\right) = \frac{G'}{G} = \frac{\beta e^{\alpha(E_{Hole}+b\Delta E)}}{\beta e^{\alpha E_{Hole}}} = e^{\alpha b \Delta E} \tag{4.1}$$

Relation of Currents

Sometimes it is not possible to calculate the amount of ions from the current measurements, but the amount of electrons and vice versa. Since the ionisation produces electrons and ions in pairs and the chamber is an isolated system, it is possible to use the inverse current of one sort of charge carriers to determine the current of the other charge carrier. Another consequence of the production by pairs is that the sum of all charges is zero, i.e. the sum of all currents must vanish.

Single GEM operation

In some calculations it is necessary to subtract the currents concerning only the first GEM from the currents caused by the second GEM. Therefore measurements are carried out where the second GEM is not operated. Instead it was used as an anode pick up with both GEM electrodes grounded. The sum of the currents from the top and bottom of the second GEM are in good approximation the same as if the GEM would be replaced by a real anode plate. With this setup, only currents related to the first GEM are recorded. In the equations these currents are denoted as I^0.

Determination of the GEM Coefficients

The GEM coefficients for the extraction and the collection of charges depend on the ratio of the electric field inside the GEM hole and the external electrical field. In the measurements the external fields are varied and the GEMs are operated at high enough voltages to get a sufficient signal height. Depending on the coefficient to be studied, different fields are varied:

- For the electron collection efficiency the drift field is varied: as it is the first field it has the highest impact and the signal is still amplified by the second GEM.

- For the electron extraction efficiency the induction field is varied, because no other charges apart from electrons are found in the induction gap and cannot disturb the currents.

- For the ion collection efficiency the transfer field is varied, as it is the only field between to GEMs.

- For the ion extraction efficiency the transfer field is varied. No other fields allow the determination of this quantity.

- For the secondary ion extraction the drift field is varied, as it is the only field above the two GEMs.

- The effective gain depends mainly on the GEM voltage, thus in these measurements the voltages across the GEMs are varied.

With these field variations the coefficients are calculated from the measured currents as follows.

Electron Collection Efficiency: The collection efficiency multiplied by the gain can be measured rather than the bare electron collection efficiency, because the electrons pulled into a GEM hole are multiplied due to the amplification. If only the drift field is varied, the change in the collection efficiency of the first GEM is related to the change of the anode current. The relative electron collection efficiency normalised to the maximum anode current I_A^{max}, is given by

$$C_{rel}^{-} = \frac{I_A/\Gamma(E_D)}{I_A^{max}/\Gamma\left(E_{D|_{I_A=I_A^{max}}}\right)} \ . \tag{4.2}$$

Electron Extraction Efficiency: The calculation of the electron extraction efficiency is straightforward. The currents from the second GEM and the anode correspond directly to the amount of charge determining the extraction of electrons. The total number of electrons produced is related to the sum of the electron currents at the bottom of the GEM and the anode. The amount of electrons extracted from the second GEM is related to the anode current. Thus, for the second GEM the extraction efficiency of electrons is given by

$$X^{-} = \frac{I_A/\Gamma(E_I)}{I_A/\Gamma\left(E_I\right) + I_{GEM2_A}/\Gamma\left(E_I\right)} = \frac{I_A}{I_A + I_{GEM2_A}} \ . \tag{4.3}$$

Here, the correction factors corresponding to the change in the induction field, are the same for all currents. As the ratio of currents is considered, the corrections are cancelled out. The same applies to the following calculations, as long as not specified otherwise.

Ion Collection Efficiency: The ion collection efficiency is obtained from the ion current, which is transferred from the second GEM to the first GEM. In principle the ions extracted from the holes of the first GEM, which are related to the sum $I_C + I_{GEM1_C}$, correspond to the amount of ions from the second GEM. But, due to the amplification process, the ions produced in the first GEM must be taken into account, too. The correlated currents are determined by a measurement, where the second GEM is not operated. Therewith, the currents concerning only the ions produced in the first GEM can be detected. These currents are subtracted from the currents, which are measured with the second GEM in operation. They are denoted as I_C^0 and $I_{GEM1_C}^0$, respectively. The ratio of the ion current collected by the first GEM and the total ion current outgo the second GEM gives the ion collection efficiency. The total ion current from the second GEM is correlated to the

total electron current produced in the second GEM, $I_A + I_{GEM2_A}$. Since not all ions are extracted from the second GEM, the ion current on the cathode side of the second GEM has to be subtracted:

$$C^+ = \frac{(I_C - I_C^0) + \left(I_{GEM1_C} - I^0_{GEM1_C}\right)}{-(I_A + I_{GEM2_A}) - I_{GEM2_C}} \tag{4.4}$$

In this proceeding it is assumed that the recombination of ions and electrons in the GEM holes is negligible, as long as the number incoming or outgoing ions is large compared to the number of electrons. This is obviously the case, because the ions from the second GEM are a result of an amplification of electrons produced in the first GEM. Thus, the ratio of the amount of charges is in the order of the amplification.

Ion Extraction Efficiency: The ion extraction efficiency for the second GEM is given by the ratio of the ion current extracted to the first GEM and the total ion current produced in the second GEM. From the considerations above follows

$$X^+ = \frac{-(I_A + I_{GEM2_A}) - I_{GEM2_C}}{-(I_A + I_{GEM2_A})} \ . \tag{4.5}$$

Secondary Ion Extraction Efficiency: The secondary extraction efficiency describes the ratio of ions from the second GEM reaching the cathode and the total number of ions collected by the first GEM. Again, to subtract the ion currents produced in the first GEM I_C^0 and $I^0_{GEM1_C}$, a reference measurement with a deactivated second GEM is done. The secondary ion extraction efficiency is

$$X^+_{sec} = \frac{I_C - I_C^0}{(I_C - I_C^0) + \left(I_{GEM1_C} - I^0_{GEM1_C}\right)} \ . \tag{4.6}$$

Effective Gain: The effective gain can be obtained from the current measurements, by calculating the ratio of the amount of primary electrons and the amplified number of electrons. Since the current from the primary ionisation is rather small and imprecisely to measure, the electron current after the first amplification is taken into account. For this the current sum $I^0_{GEM2_C} + I^0_{GEM2_A}$, which is collected by the deactivated and grounded second GEM is used as the primary current:

$$G_{eff} = \frac{I_A + I_{GEM2_A}}{I^0_{GEM2_C} + I^0_{GEM2_A}} \ . \tag{4.7}$$

Here, the recombination in the transfer gap by ions output by the second GEM is no longer negligible. The amount of primary electrons decreases and the effective gain is expected to be smaller than that from measurements using other techniques to obtain the gain of GEMs [27].

Ion Feedback: The ion feedback IF cannot be determined as it was defined in Section 2.3.2. Due to the recombination, the total number of ions produced is not measurable. However, two different approaches are used to obtain an ion feedback from the current measurements. The first equation is taken from [40] and estimates the total number of ions by the number of electrons reaching the anode. This approach is an inverse signal to noise relation, where the ion feedback is considered as the noise. If the gain is know, this relation reveals whether the ion feedback is of the same order as the primary ionisation. In the sense of the definition, here the ion feedback is overestimated, because the total number of ions produced is larger than the number of electrons reaching the anode:

$$IF = \frac{I_C}{I_A} \ . \tag{4.8}$$

In [21] the ion feedback is calculated, using all measurable ion currents. The sum of these currents is then regarded as the total number of ions.

$$IF = \frac{I_C}{I_{GEM2_C} + I_{GEM1_C} + I_C} \tag{4.9}$$

Again, the ion feedback is overestimated, but in comparison to Equation 4.8 the ions collected by the GEMs are also taken into account. Although, this approach does not reflect that the number of ions produced in the GEM holes is higher than the considered ion currents on the upper GEM electrodes. Since the second approach is ascribed to the definition of the ion feedback, for the calculations of the ion feedback Equation 4.9 is used.

4.3 Systematical Errors

In the following the systematic errors of the measurements are discussed. An overview of the results in this section is given in Table 4.1.

High Voltage Supply

The voltages, supplied by the high voltage system SY127, are monitored with an accuracy of $\sigma_V/V \sim 0.3\%$ [41].

Distances

The distances between the electrodes are adjusted with distance pieces (5 mm) and washers (0.5 mm). They have an accuracy of ±0.1 mm and ±0.01 mm, respectively. The height of the GEM frames (1mm) has a relative large error of ±0.1 mm, owing to the uncertainty in the amount of glue used to stick the GEM foil into the frame. The thickness of the copper tin (1 mm) used for the rings has an error of ±0.01 mm in height. For the estimation of the maximum overall error, the error of the distance between the second ring and the first GEM is used. It is calculated with an uncertainty of two GEM frames, five washers and one distance piece. The total error is $\sim \pm 0.20$ mm and related to the distance of 3.5 mm this leads to a relative error of $\sigma_{Distance}/Distance \sim 6\%$.

Electrical Fields

According to the errors from the distances and the high voltage supply, the relative error $\sigma_{E_{ext}}$ for the electrical fields between the electrodes is calculated to

$$\frac{\sigma_{E_{ext}}}{E_{ext}} = \sqrt{\left(\frac{\sigma_V}{V}\right)^2 + \left(\frac{\sigma_{Distance}}{Distance}\right)^2} \sim 6\% \ . \tag{4.10}$$

For the electrical field inside the GEM hole, following Equation 2.19, the relative error $\sigma_{E_{Hole}}/E_{Hole}$ is given by

$$\frac{\sigma_{E_{Hole}}}{E_{Hole}} = \sqrt{\left(\frac{\sigma_a}{a}\right)^2 + \left(\frac{\sigma_V}{V}\right)^2 + \left(\frac{\sigma_b}{b}\right)^2 + \left(\frac{\sigma_{E_D}}{E_D}\right)^2 + \left(\frac{\sigma_{E_I}}{E_I}\right)^2} \sim 9\% \ . \tag{4.11}$$

Finally, the error for the ratio of the electrical field inside the GEM hole and an external field $\sigma_{E_{rel}}/E_{rel}$ is around 11%.

Current Measurements

The errors in the current measurements are governed by the statistical fluctuations in readings from the CUMOs, systematical errors of the CUMOs and systematic errors made by the ADC in conversion.

The statistical errors happen at a time scale of one second and are of the order of a few percent of the value. They are assumed to be electronic noise from the devices and wire connections. By averaging the current values, these uncertainties can be reduced. The arithmetical averaging is controlled by the computer based readout system and typically carried out with ten measurements.

The systematics for the CAMAC readout system σ_I are discussed in [26]. There, the error of the CUMOs is estimated to 1%, whilst the error given by the ADC is found to be dependent upon the maximum possible current for a given range I_{max}. The overall systematical error is given by $\sigma_I/I = I_{max}/I \cdot 818 + 0.01$.

For the new developed USB readout system a calibration was done. Therefore, the systematical error is given by the error from the calibration fit (see Section 5.1.1). From the standard deviation obtained from the gnuplot fitting routine the relative error is given by $\sim 0.2\%$.

Quantity	Denotation	Error
External field strength	$\sigma_{E_{ext}}/E_{ext}$	6%
Field strength in GEM hole	$\sigma_{E_{Hole}}/E_{Hole}$	9%
Ratio of external and hole field strength	$\sigma_{E_{rel}}/E_{rel}$	11%
Currents taken with CAMAC readout	σ_I/I	$\frac{I_{max}}{I*818} + 0.01$
Currents taken with USB readout	σ_I/I	0.2%

Table 4.1: Overview of the systematical errors.

Chapter 5

Results and Discussion

In this chapter the results from the measurements are presented. This includes the calibration of the readout system as well as the tests of the operation of the detector chamber and the measurements of the GEM coefficients.

5.1 Preparative Experiments

Before the measurements of interest could be performed, several preparative experiments were carried out to test the stability of the chamber and the new data acquisition had to be calibrated. The results of these experiments are described in the following

5.1.1 Calibration of the USB Readout System

The calibration of the USB readout system was carried out with a Keithley 6514 amperemeter. Currents through high resistors (100 MΩ - 1 GΩ) are measured with both the CUMO amperemeters and the Keithley 6514. The resulting voltages from the monitoring connectors of the CUMOs are digitised by the ADC and recorded with the data acquisition software. Plotting the currents from the Keithley amperemeter versus the recorded voltages yields the calibration curve. A linear function is fitted to the data, which reveals the calibration factors for the conversion of voltages to currents, which is performed later by the software. The results for all ranges of the CUMOs are shown in Fig. 5.1 and Fig. 5.2. The fit is done by the gnuplot fit routine and the resulting fit parameters are printed in the graphs. As mentioned in the discussion about the systematical errors (Section 4.3), the maximum relative standard deviation from the fits is 0.2%.

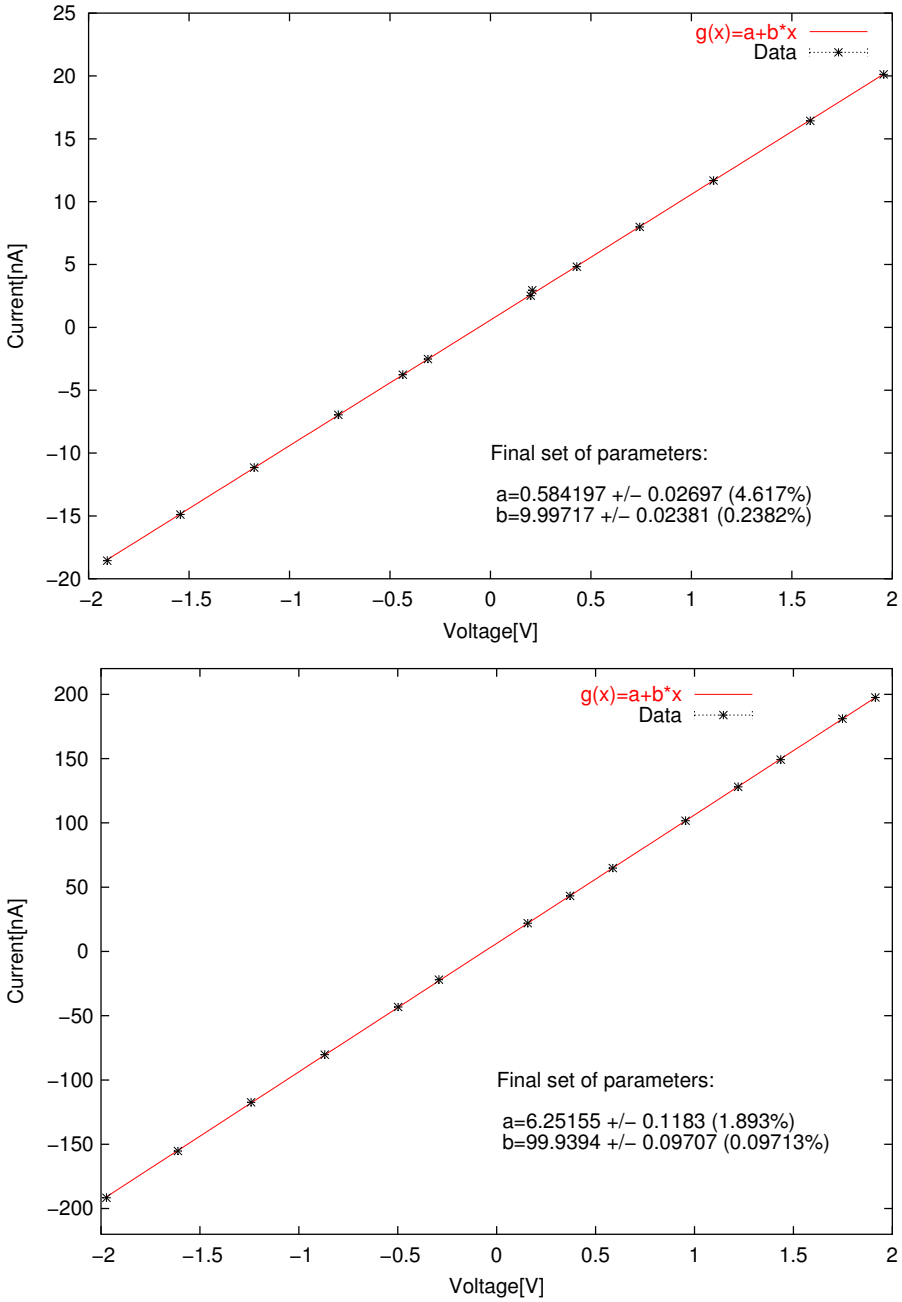

Figure 5.1: Results from calibration of the readout system for the current ranges of 20 nA and 200 nA. The currents measured with a Keithley 6514 are taken as reference and plotted versus the recorded voltages.

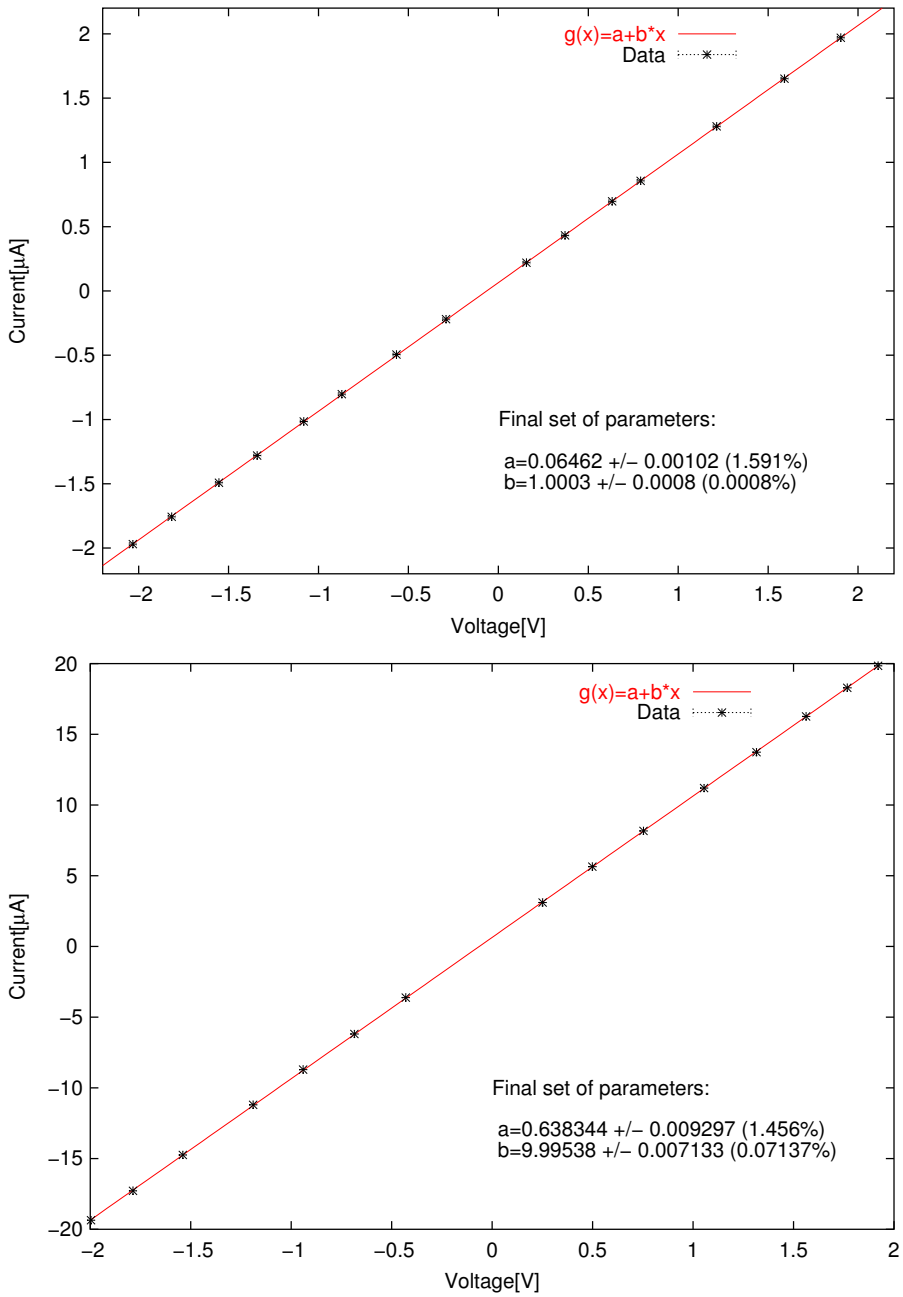

Figure 5.2: Results from calibration of the readout system for the current rangse of 2 μA and 20 μA. The currents measured with a Keithley 6514 are taken as reference and plotted versus the recorded voltages.

5.1.2 Steady Currents

In order to examine, whether the currents on the electrodes are constant, when no changes to the system are made, the currents from each of the electrodes was monitored over average period of 10 minutes. Constant currents at the electrodes indicate that stable conditions, e.g. high voltage stability, have been achieved and parameters such as gas pressure and temperature are well under control. In Figure 5.3 a plot with the currents on all electrodes, which are later included into the calculations, is shown.

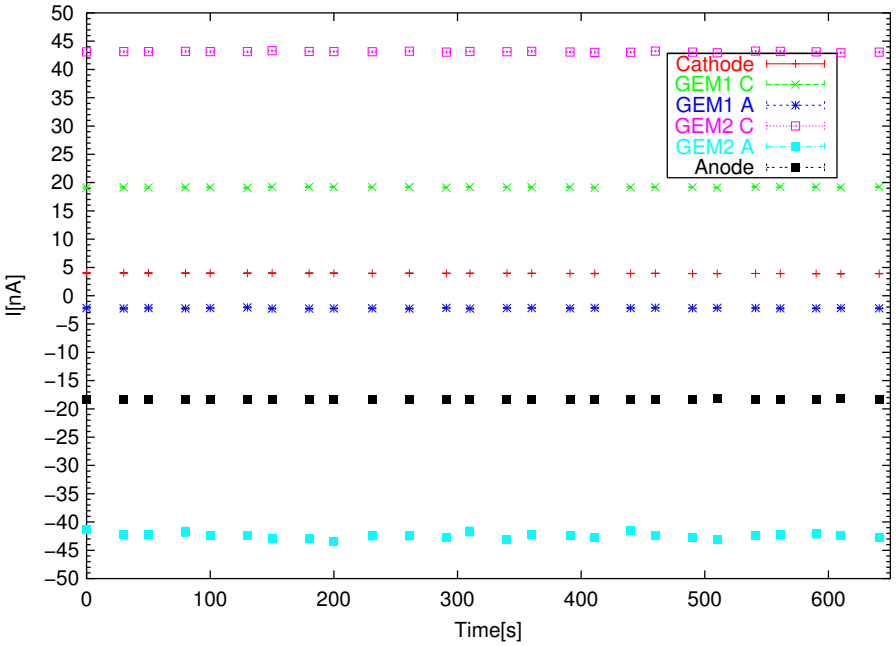

Figure 5.3: Graph of the currents of all electrodes included into the calculations. The currents stay constants, as no changes to the system are made.

5.1.3 Current Sum

Besides tests for high voltage stability and tests of the gas amplification, when high enough voltages are applied to the GEMs, it is a major significance for the correct operation of the chamber that the current sum vanishes. This indicates that the system is isolated and the measurements are not distorted. Since not all charges are produce in regions where the current measurements are sensitive to, e.g. the chamber wall, the current sum is only determined

for the charges produced in the volume between the cathode and the anode, in particular the volume above and below the GEMs.

The currents are measured with the high voltage applied and the iron source in the position where it irradiates the drift volume. The sum of all currents from the cathode, anode and GEM surfaces is plotted in Fig. 5.4. Within the errors the current sum is almost zero, this means no charges are lost in the sensitive volume.

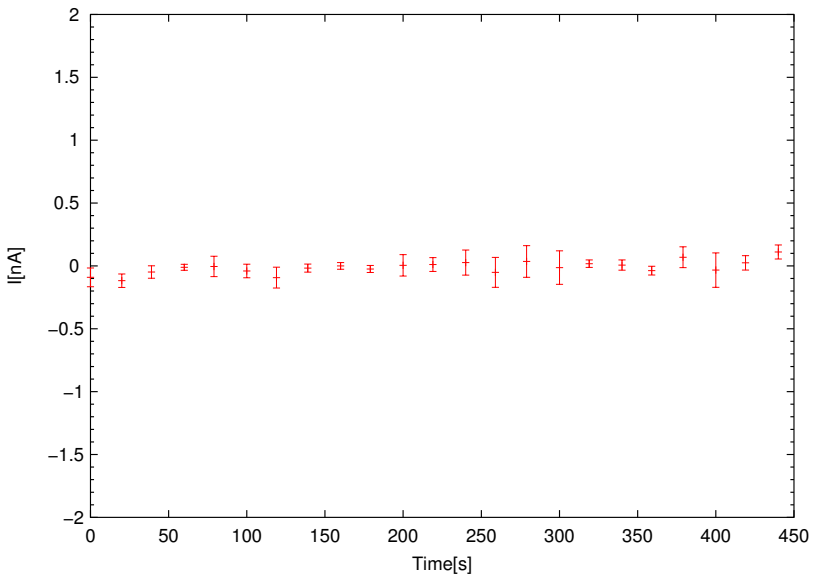

Figure 5.4: Graph of the sum of the currents on the cathode, anode and GEM surfaces. During the duration of the measurement no changes either to the fields nor to the GEM voltages are applied. This data was taken with the two ring GEM tower.

However, with the first GEM tower employing only one field cage ring, it was found that the currents did not sum to zero (see Fig. 5.5). One particular measurement gave the average net current as (0.278±0.010) nA. This positive value means that electrons are lost on surfaces, where the current measurements are not sensitive, e.g. the grounded chamber walls.

It was hypothesised that this was due to edge effects, since the ^{55}Fe source has a radiation length of $\sim$ 2 cm, whilst the distance between the drift region and the window in the chamber vessel is 4 cm. This means that the intensity of the photon beam is significantly lower in the centre of the GEM tower. The highest radiation intensity occurs on the edges of the GEM tower where the electric field is least homogeneous. This region, in which the largest number of ions and electrons are produced, is an area where charges most likely to

be lost. From the simulations (see Fig. 3.5) follow, this inhomogeneity has an extension of around 6 mm. Ions produced in this region are still attracted by the cathode, whereas the corresponding electrons are lost to surfaces not read out by the amperemeters.

The non zero current sum does not pose a problem for measuring the GEM coefficients, since the currents measured are high due to amplification. Though, for the measurement of ion feedback, where the ion current in the drift region is ofthe order of a few nanoampere, a net current adds an error of approximately 10%.

To improve the current sum, two solutions were considered. First a radioactive source with a longer radiation length, such as ^{90}St (Strontium), could be used, leading to more ionisation in the centre of the drift volume. This would increase the total current and hence, the field distortions at the edges would have not such high impact. Unfortunately a source with a high enough rate was not available. Thus, only the second approach was realised. As the simulations show (see Fig. 3.5) a significant improvement in the field homogeneity, a second ring was added to the GEM tower design. As shown above the current sum with a GEM tower built with two rings has no permanent offset and within the errors the current sum vanishes.

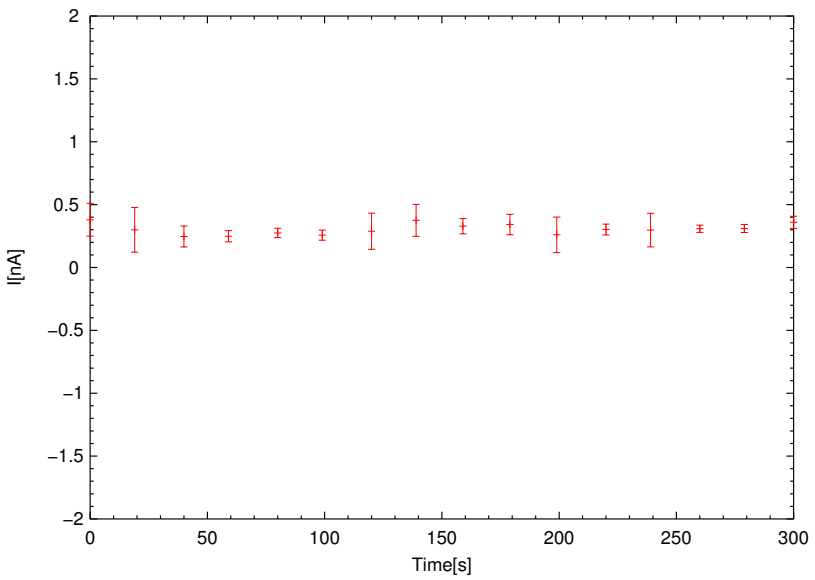

Figure 5.5: Graph of the sum of the currents on the cathode, anode and GEM surfaces. The data on which this plot is based was taken with the one ring GEM tower.

5.2 Measurements of GEM coefficients

The GEM coefficients are calculated from the currents measured as introduced in Section 4.2.2. The following measurements are performed with Standard-GEMs manufactured at CERN. Fig. 5.6 shows a graph of currents from all relevant electrodes as they vary with increasing induction field. The graph shows the magnitude of the currents measured at each of the electrodes.

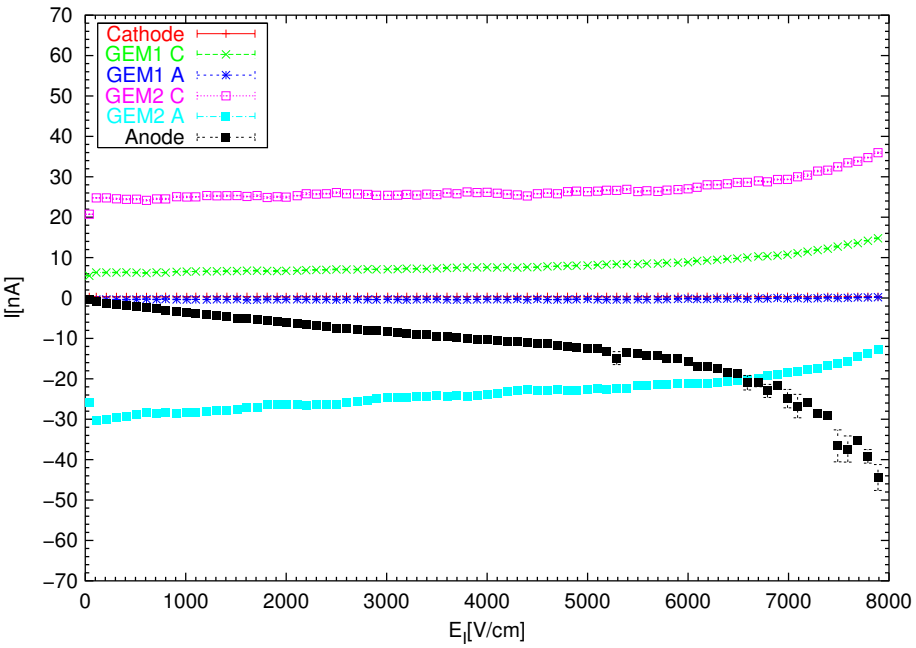

Figure 5.6: Currents on all electrodes when the induction field is varied.

From this plot, in principle, the characteristic of GEMs can be deduced. Here, in particular, the anode current increases, whilst the current on the bottom of GEM2 decreases, as more electrons are extracted to the anode with increasing induction field strength. In the following, however, the GEM coefficients are plotted as functions of the field ratios. This is more conclusive, as it includes the variation of the GEM voltage into the considerations.

5.2.1 Electron Collection Efficiency

The graph in Fig. 5.7 shows the electron collection efficiency obtained using Eq. 4.2. The parameters for the measurements are summarised in Table 5.1.

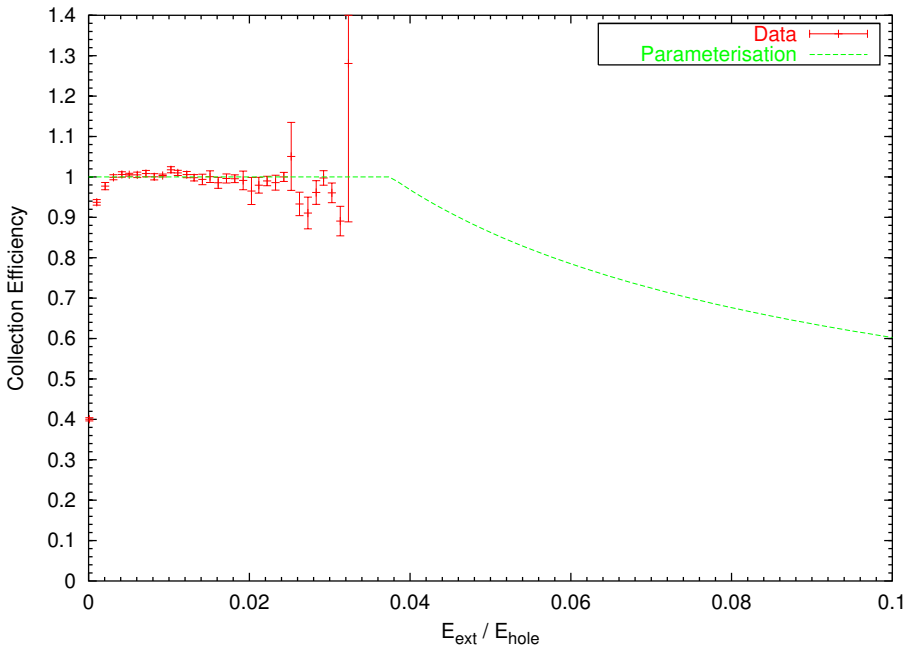

Figure 5.7: Electron Collection Efficiency compared to the parameterisation.

The results are in good agreement with the parameterisation using the parameters from the simulations (see Table 2.1). Only a deviation for a very low drift field is apparent, where, owing to recombination of electrons and ions, the collection efficiency decreases strongly. This is not taken into account in the parameterisation. This affect is also observed in [24, 26].

For high external fields problems occurred at the cathode electrode. The current on the cathode increased owing to dark currents on the surfaces of the GEM tower support structures and the high voltage supply tripped permanently.

The maximum electron collection efficiency is reached when a low drift field is present. However, the size of the drift field is dictated by the maximum drift velocity of the electrons. Fortunately, this is the case for fields in the order of 100 V/cm. Thus, with a reasonable adjusted GEM voltage for the first GEM, both a high drift velocity and a good electron collection efficiency can be exploited.

5.2.2 Electron Extraction Efficiency

The electron extraction efficiency is shown in Fig. 5.8. The coefficient is calculated from the measured currents using Eq. 4.3. An agreement between

	Field Strength, GEM Voltage
E_D	0...5000 V/cm
U_{GEM1}	320 V
E_T	2000 V/cm
U_{GEM2}	320 V
E_I	2000 V/cm
Gas Mixture	Ar-CH_4-CO_2 (93:5:2)

Table 5.1: Parameter for the electron collection efficiency measurement.

the measurement and the parameterisation for E_{ext}/E_{hole} lower than 0.1 is visible. The rise of the extraction efficiency occurs as a result of ionisation in the induction gap, when the field energy of the induction field exceeds the ionisation potential of the gas mixture, which is not taken into account by the parameterisation.

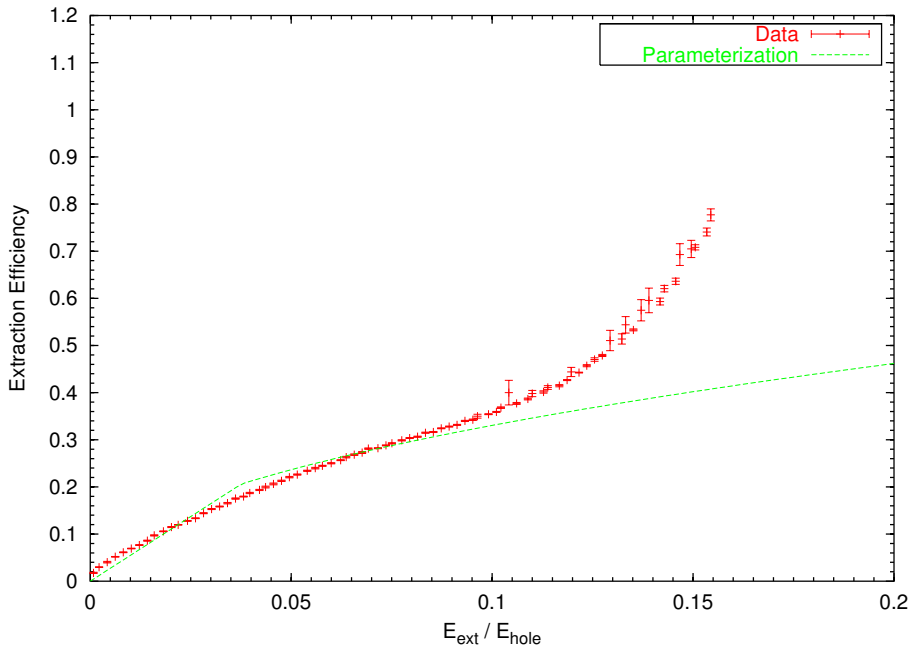

Figure 5.8: Electron Extraction Efficiency compared to the parameterisation.

However, at the beginning of the measurements no reasonable results were obtained. As shown in Fig. 5.9, the extraction efficiency was much to high and the ionisation in the induction gap occurs at a much lower field strength. In contrast to the high extraction efficiency, which theoretically is

explainable by a different GEM geometry, the fact that the onset of the ionisation in the induction region occurred at a field strength around 3500 V/cm was not expected. The ionisation takes place at field strengths higher than 7000 V/cm [40]. This failure was due to a convex shape of the anode. An assumption to explain this change of shape, is that the anode was a composite of two plates glued together and owing to bimetal effects, the shape of the anode plate was distorted. This effect decreased the induction gap by approximately 1 mm, yielding an error of 50% for both, the distance and the field strength. Therefore, the anode was replace by a single layer copper covered plate.

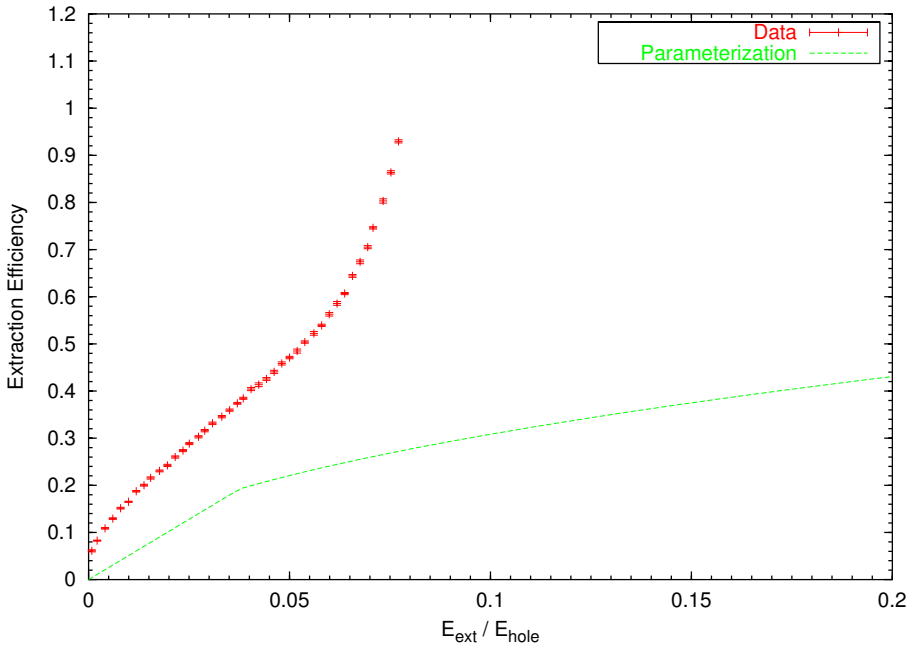

Figure 5.9: Electron Extraction Efficiency compared to the parameterisation. The data is taken with the convex shaped anode.

The parameters for the measurements are summarised in Table 5.2.

5.2.3 Ion Collection Efficiency

The graph for the ion collection efficiency, calculated from the measurements using Eq. 4.4, is shown in Fig. 5.10. In this measurement, the transfer field was varied, Table 5.3 gives an overview of the used parameters. The measurements generally follow the parameterisation. The collection efficiency for

	Field Strength, GEM Voltage
E_D	250 V/cm
U_{GEM1}	320 V
E_T	2000 V/cm
U_{GEM2}	320 V
E_I	0...8000 V/cm
Gas Mixture	Ar-CH_4-CO_2 (93:5:2)

Table 5.2: Parameter for the electron extraction efficiency measurement.

ions is, compared to electrons, slightly higher, which is explainable by the minor diffusion owing to the larger ion masses.

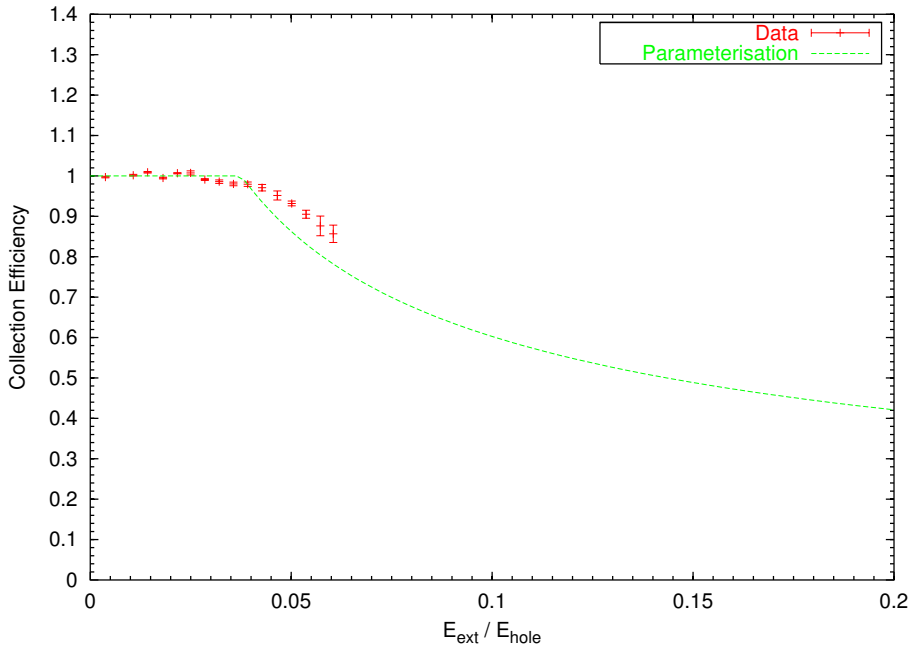

Figure 5.10: Ion Collection Efficiency compared to the parameterisation.

The plot shows that with increasing external field, more ions are neutralised at the GEM surface instead of being collected into the holes. Since for higher field strength, more field lines end up on the GEM surface (see Fig. 2.14), this is expected. With respect to the number of ions reaching the cathode, these results suggest a high transfer field to minimise the ion feedback.

	Field Strength, GEM Voltage
E_D	250 V/cm
U_{GEM1}	360 V
E_T	0...5000 V/cm
U_{GEM2}	360 V
E_I	3500 V/cm
Gas Mixture	Ar-CH_4 (95:5)

Table 5.3: Parameter for the ion collection efficiency measurement.

5.2.4 Ion Extraction Efficiency

The same data recorded for the collection efficiency of ions by varying the transfer field is analysed to obtain the extraction efficiency of ions. The parameters of the measurement are summarised in Table 5.3 and the coefficient is calculated using Eq. 4.5. In Fig. 5.11 the resulting plot is shown together with the parameterisation. As for the electron extraction efficiency, the ion extraction follows the parameterisation. Here, because of the short distances ($\sim$ 50 μm), the differences in diffusion and drift velocity have no significant effect.

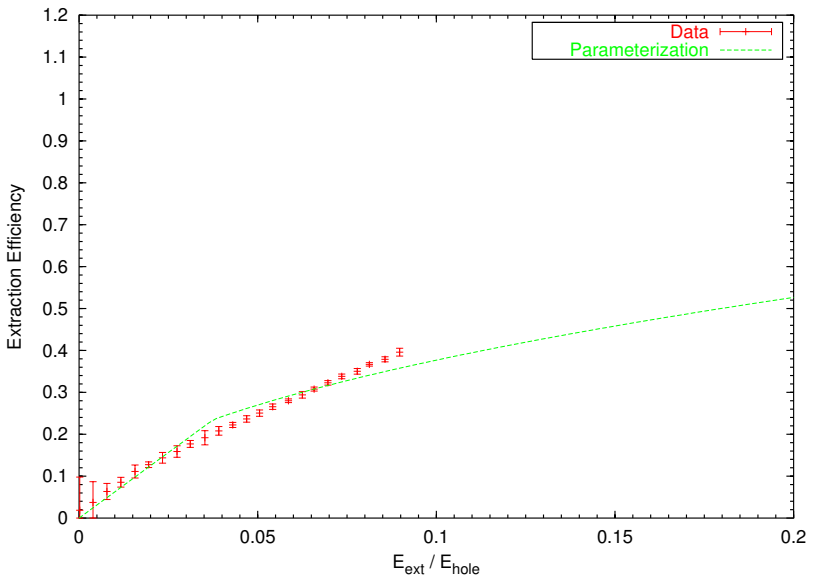

Figure 5.11: Ion Extraction Efficiency compared to the parameterisation.

According to an increasing field strength, fewer field lines from the GEM

holes end on the surface of the second GEM. Thus, more ions are pulled to the first GEM and the extraction efficiency increases. To achieve a desired low ion extraction efficiency, the plot suggests that a low transfer field is optimal. However, the preferred low transfer field is in contrast to the high transfer field required for a low ion collection efficiency of the first GEM. Here, the GEM voltages can be used to avoid this contradiction, because the ratio of field strengths is the deciding factor.

For the first GEM it is important to achieve a very low ion extraction efficiency. This is realised by a low drift field, which is obligatory for the required maximum drift velocity.

5.2.5 Ion Feedback

In Fig. 5.12 the ion feedback obtained from the data recorded for the measurements of the electron collection efficiency is shown. The ion feedback is calculated using Eq. 4.9 and plotted against the drift field. For a low drift field strength the ion feedback is suppressed to 1% of the total amount of produced ions. The plot shows a linear behaviour, which is expected, as in this measurement the ion feedback is only affected by change of the ion extraction of the first GEM, which changes linearly.

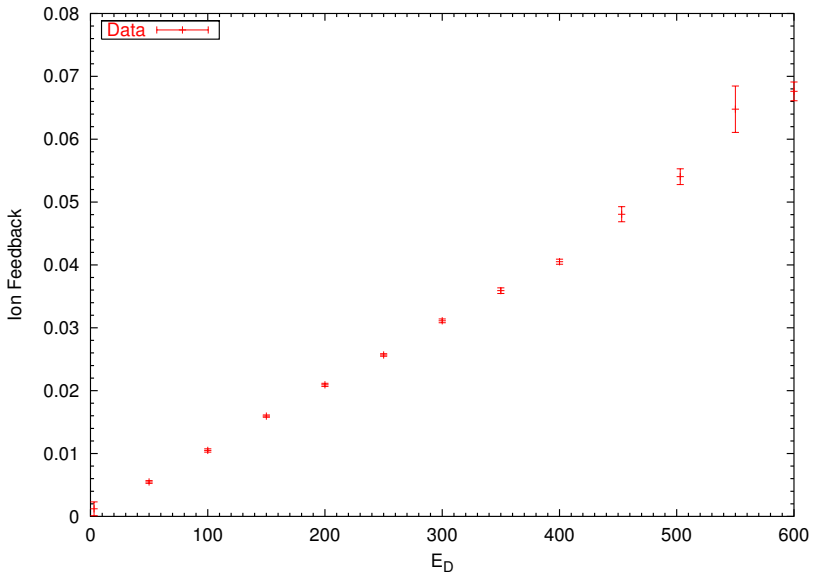

Figure 5.12: The ion feedback plotted against the drift field strength.

From this measurement it can be seen, that, in order to reduce the ion feedback to the desired amount of 10^{-4}, an optimised setting of GEM voltages

and field strengths is necessary. Though, no systematic studies have been performed, it can be said, that a low drift field is mandatory. In addition, a low amplification of the first GEM is reasonable, since the amount of ions produced in the first GEM should be as low as possible. A low transfer field decreases the amount of ions extracted from the second GEM, which in principle also decreases the ion feedback. However, with a low transfer field the electron extraction efficiency of the first GEM is also decreased and the number of electrons reaching the second GEM would be very low. In order to obtain a high signal on the readout pads, the induction field and the voltage across the second GEM should be as high as possible. As the suggested low voltage across the first GEM demands a very high gain of the second GEM, the operational stability of the second GEM can be a problem. To avoid this, a triple GEM readout can be used. There the main amplification can be produced by two GEMs.

5.3 Russian GEMs

In the following the result from measurements carried out with Russian GEMs is presented. In Fig. 5.13 the relative anode current is plotted against the GEM voltages. The voltages across the GEMs are changed simultaneously. Since the scale for the current is logarithmic, the apparent linear dependency reveals an exponential increase of the anode current with increasing GEM voltages. This is the expected behaviour and confirms the correct operation of the employed Russian GEMs.

Unfortunately no other conclusion than the verification of the operation of the Russian GEMs can be drawn. From the measured data no prediction of the absolute gain can be obtained, as the setup for this measurement impeded further calculations.

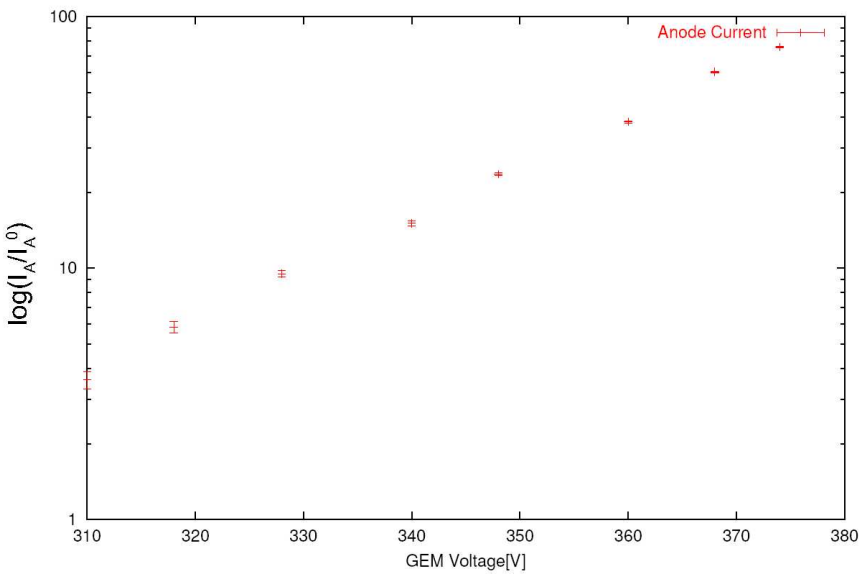

Figure 5.13: The anode current plotted against the GEM Voltages. The anode current is normalised to a current at a GEM voltage of 250 V.

Chapter 6

Summary and Outlook

For the studies of a GEM based gas amplification system for a possible Linear Collider TPC a setup was built. A new detector was installed for the investigation of charge transfer processes of a GEM based TPC. In addition an existing current readout system was partly rebuilt and a software data acquisition was implemented for systematic studies of GEM properties. The operativeness of the detector was verified and improvements to the GEM tower design were made. During the setup construction first measurements were performed. They are in good agreement with already published studies [23, 24, 26]. Hence, the test setup seems to fulfil the requirements for the investigation of GEMs.

The measurements are encouraging for a GEM based gas amplification for the readout of a TPC. Furthermore, the results give a hint, that, with a well adjusted field configuration, the operation properties of a TPC can be improved and the intrinsic ion feedback of GEMs can be successfully exploited. However, more detailed investigations are necessary to gather more knowledge about the characteristics of GEM based gaseous detectors. Therefore, the studies of the charge transfer coefficients have to be continued for different GEM types, as well as for different gases and a wide range of field configurations.

In preliminary measurements the operation of GEMs in high magnetic fields was verified, though no reliable results were obtained. The studies in magnetic field environment are still outstanding and planned for the near future. This is of major interest, as the TPC for the Linear Collider will be operated in a high magnetic field of 4 Tesla.

Furthermore, GEMs manufactured by a Russian company were successfully operated, but here no results of the charge transfer properties were obtained. There are developments in the manufacturing of GEMs and it is necessary to compare the GEMs produced by different manufactures. A first

step was done by employing the Russian GEMs. The flexible design of the chamber allows to use various kinds of GEMs, as long as they are provided in a suitable supporting frame. For the future detailed studies of the Russian GEMs are planned.

Appendix A

A.1 Physical Data

A.1.1 Radioactive Source

Nuclide	:	^{55}Fe
Half-life time	:	2.7 a
Energy	:	5.89 keV (24%)
		6.49 keV (2.9%)

A.1.2 Radiation Length

Material	:	Argon
Mass absorption coefficient	:	$2.73 \cdot 10^{2}$ cm^2/g
Density	:	$1.784 \cdot 10^{-3}$ g/cm^3

The radiation length under normal conditions for a photon with an energy of 5.89 keV is $\sim$ 20.5 mm.

A.2 Multiplexer Circuit

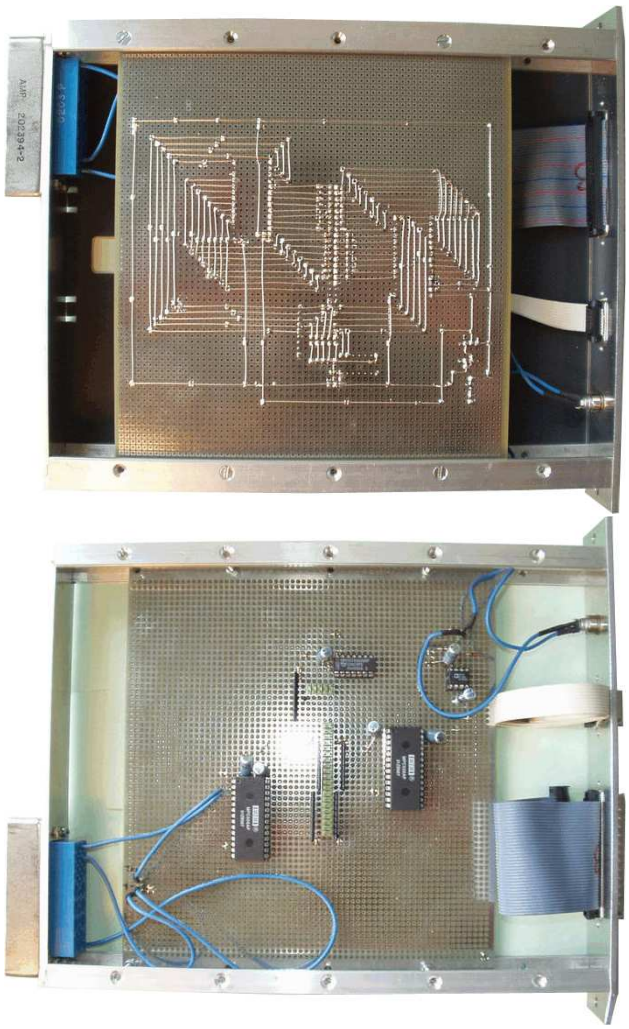

Figure A.1: Photographs of the soldered multiplexer circuit. On the backside of the circuit board the wiring of the electronic components is visible. The components are placed on the frontside to shield them from the signals of the wires.

Bibliography

[1] F. Richard, J. R. Schneider, D. Trines, and A. Wagner: *TESLA Technical Design Report Part I: Executive Summary* (2001). DESY-01-011, `hep-ph/0106314`.

[2] R. Brinkmann *et al.*: *TESLA: The Superconducting Electron Positron Linear Collider with an integrated X-ray Laser Laboratory Technical Design Report. Pt. 2: The Accelerator.* DESY-01-011.

[3] J. A. Aguilar-Saavedra *et al.*: *TESLA Technical Design Report Pt 3: Physics at an e^+e^- Linear Collider* (2001). DESY-01-011, `hep-ph/0106315`.

[4] T. Behnke, S. Bertolucci, R. D. Heuer, and R. Settles: *TESLA: The Superconducting Electron Positron Linear Collider with an integrated X-ray Laser Laboratory. Technical Design Report. Pt. 4: A Detector for TESLA.* DESY-01-011.

[5] T. Abe *et al.* (American Linear Collider Working Group): *Linear Collider Physics Resource Book for Snowmass 2001. 1: Introduction* (2001). `hep-ex/0106055`.

[6] N. Akasaka *et al.*: *JLC Design Study.* KEK-REPORT-97-1.

[7] W. Demtroeder: *Experimental Physik IV.* Springer-Verlag (1998).

[8] K. Hagiwara *et al.* (Particle Data Group): *Review of particle physics.* Phys. Rev. **D66**(2002) 010001.

[9] M. Hauschild *et al.*: *Particle Identification with the OPAL Jet Chamber.* Nucl. Instrum. Meth. **A314**(1992) 74.

[10] *X-Ray Data Booklet* 2nd *Edition* (2001). http://xdb.lbl.gov.

[11] W. Blum and L. Rolandi: *Particle Detection with Drift Chambers.* Springer-Verlag (1993).

[12] E. Rapkin: http://www.inus.com/docs/gcinfo.htm.

[13] D. R. Nygren: *A Time Projection Chamber*. Presented at the 1975 PEP Summer Study. Included in Proceedings.

[14] http://www.star.bnl.gov/STAR/html/tpc_l/tpc.html.

[15] A. Breskin *et al.*: *High flux Operation of the Gated Multistep Avalanche Chamber*. Nucl. Instr. Meth. **178**(1980) 11.

[16] F. Sauli: *GEM: A new Concept for Electron Amplification in Gas Detectors*. Nucl. Instrum. Meth. **A386**(1997) 531.

[17] http://gdd.web.cern.ch.

[18] M. Hamann: *Studies for a Linear Collider Drift Chamber and Search for Heavy Stable Charged Particles in e^+e^- Collisions up to $\sqrt{s} = 209 GeV$* (2003). DESY-THESIS-2003-046.

[19] F. Sauli and A. Sharma: *Micropattern Gaseous Detectors*. Ann. Rev. Nucl. Part. Sci. **49**(1999) 341.

[20] Y. Giomataris, P. Rebourgeard, J. P. Robert, and G. Charpak: *Micromegas: A High-Granularity Position-Sensitive Gaseous Detector for High Particle-Flux Environments*. Nucl. Instrum. Meth. **A376**(1996) 29.

[21] S. Bachmann *et al.*: *Charge amplification and transfer processes in the gas electron multiplier*. Nucl. Instrum. Meth. **A438**(1999) 376.

[22] M. Killenberg *et al.*: *Modelling and measurement of charge transfer in multiple GEM structures*. Nucl. Instrum. Meth. **A498**(2003) 369. `physics/0212005`.

[23] B. Sobloher: *Simulationsstudien zu GEM-Folien fuer die Auslese einer TPC* (2002). III. Physikalisches Institut, RWTH Aachen.

[24] S. Bachmann *et al.*: *Operation properties of detectors base on GEM*. Proc. Int. Workshop on Micro-Pattern Gas Detectors, Orsay (1999).

[25] A. Sharma: *3D simulation of Charge Transfer in a Gas Electron Multiplier (GEM) and Comparison to Experiment*. Nucl. Instrum. Meth. **A454**(2000) 267.

[26] S. Lotze: *Aufbau eines Teststandes und Messungen zum Betrieb einer TPC mit GEMs* (2001). III. Physikalisches Institut, RWTH Aachen.

[27] T. Lux: *Bau und Test einer Mini-TPC mit GEM-Auslese zur Messung des Ionen-Rueckflusses* (2001). Inst. f. Exp.Physik, Universitaet Hamubrg.

[28] *Maxwell® Student Version*. http://www.ansoft.com/maxwellsv.

[29] *C.A.E.N. SY127 High Voltage System Users Manual* (1991). http://www.caen.it/nuclear/getattach.php?mod=SY127.

[30] F. Beissel: *Handbuch zum HV Current Monitor, Revision V3.0* (1999). III. Physikalisches Institut, RWTH Aachen.

[31] *Handbuch zu Dornier CAMAC ADCs Do 200-1003/6/9, 200-1103/6/9*. Friedrichshafen.

[32] *LabJack U12 User's Guide*. http://www.meilhaus.com.

[33] *Burr Brown MPC506 datasheet* (1998). http://www-s.ti.com/sc/ds/mpc506.pdf.

[34] A. Nowack: *HV Channel Control Class, Version 1.2* (1999). III. Physikalisches Institut, RWTH Aachen.

[35] O. Streicher: *The Camac on Linux Page*. http://www-zeuthen.desy.de/∼ole/camac.

[36] *The Java Technology*. http://www.java.sun.com.

[37] *LabJackJava*. http://www.teravation.com/products.html.

[38] *Java Communication API*. http://java.sun.com/products/javacomm.

[39] *Gnuplot Central*. http://www.gnuplot.info.

[40] S. Lotze and P. Wienemann: *Measurement of Charge Transfer in GEM Structures in High Magnetic Fields*. http://www-flc.desy.de/flc/science/tpc_web/.

[41] A. Nowack: *Steigert eine Gas-Elektron-Vervielfachungsfolie die Betriebssicherheit eines Mikrostreifendetektors?* (1998). PITHA 98/30, RWTH Aachen.

[42] C. Liu: *An Investigation into the Charge Transfer Processes of a Time Projection Chamber based on Gas Electron Multipliers* (2003). Imperial College Lodon.

Danksagung

Diese Arbeit wäre ohne die Mithilfe vieler lieber Mitmenschen nicht zustande gekommen. Ich möchte mich bei allen, die mir diese Arbeit ermöglicht und zu derem Gelingen beigtragen, mich ermutigt, unterstützt und mir geholfen haben, von ganzem Herzen danken. Ihr habt mir die Möglichkeit gegeben mich selbständig zu entwickeln und meinen Weg zu gehen. Dabei habt ihr mich geleitet und den nötigen Rückhalt gegeben. Am Ende möchte ich sagen, ich hatte sehr viel Spaß und ich habe sehr viel gelernt. Ich verneige mich vor Euch in Dankbarkeit und Anerkennung und hoffe, dass ich das was ihr mir gegeben habt an andere weitergeben kann.

Die einzige Stärke,
die der Mensch braucht ist Geduld.
Sri Sathya Sai Baba

Hiermit versichere ich diese Arbeit selbstständig unter Verwendung der angegebenen Quellen und Hilfsmittel angefertigt zu haben.

Hamburg, den 5. April 2004

Bernhard Voigt